Available online at www.sciencedirect.com
ScienceDirect
Coordination Chemistry Reviews 251 (2007) 379–400
COORDINATION CHEMISTRY REVIEWS
www.elsevier.com/locate/ccr

Review

Electronic structures of exchange coupled trigonal trimeric Cu(II) complexes: Spin frustration, antisymmetric exchange, pseudo-*A* terms, and their relation to O_2 activation in the multicopper oxidases

Jungjoo Yoon, Edward I. Solomon *

Department of Chemistry, Stanford University, 333 Campus Drive, Stanford, CA 94305, United States

Received 12 December 2005; accepted 8 April 2006
Available online 25 April 2006

Contents

Abstract

Exchange coupled trinuclear Cu(II) clusters are of great importance in magnetic materials as well as in key steps of biological catalysis. However, the physical origins of the unique magnetic and spectroscopic features have been elusive and detailed descriptions of their electronic structures have been limited. In this review, we review our recent spectroscopic studies on structurally well-defined trinuclear Cu(II) model complexes with distinct Cu–O bridged structures that represent the $4e^-$ reduced, native intermediate in the catalytic reactivity of the multicopper oxidases. Our studies mainly based on electron paramagnetic resonance (EPR) and magnetic circular dichroism (MCD) experiments provide new insights into the metal–ligand bonding interactions in the ground and excited states of the exchange coupled Cu(II) trimers: (1) the *spin frustrated* ground state of an antiferromagnetically coupled Cu(II) trimer undergoes zero-field splitting into two doublet states via a first-order spin–orbit coupling effect, termed *antisymmetric exchange*, that requires effective ground-to-excited state superexchange interactions, and (2) the ligand-to-metal charge transfer excited states undergo coupling interactions via either metal- or ligand-based, single-centered spin–orbit coupling mechanisms. The former is reflected in extremely unusual ground state EPR spectral features, while the latter is manifested in the MCD spectrum of the excited states as a set

Abbreviations: CD, circular dichroism; CT, charge transfer; DFT, density functional theory; EPR, electron paramagnetic resonance; HDVV, Heisenberg, Dirac, Van Vleck; MCD, magnetic circular dichroism; MO, molecular orbital; NI, native intermediate; PI, peroxy intermediate; SOC, spin–orbit coupling; T1, type 1; T2, type 2; T3, type 3; XAS, X-ray spectroscopy; VTVH MCD, variable-temperature variable-field magnetic circular dichroism; ZFS, zero-field splitting

* Corresponding author. Tel.: +1 650 723 9104; fax: +1 650 725 0259.
E-mail address: edward.solomon@stanford.edu (E.I. Solomon).

0010-8545/$ – see front matter
doi:10.1016/j.ccr.2006.04.012

of two field- and temperature-dependent MCD *C*-terms with opposite signs. This MCD feature, called a *pseudo-A term*, has allowed differentiation of geometrically distinct Cu–O chromophores of the two model complexes and determination of the structure of the native intermediate in the reduction of O_2 to H_2O by the multicopper oxidases. The fundamental descriptions of the electronic structures of exchange coupled Cu(II) trimers implicate their significant roles in the catalytic reductive cleavage of O–O bonds in biology and in the physical properties of magnetic materials.

Keywords: Trinuclear copper cluster; Spin frustration; Antisymmetric exchange; Anisotropic exchange; Spin–orbit coupling; Multicopper oxidase

1. Introduction

Trinuclear Cu clusters with trigonal symmetry have attracted significant interest, particularly, as these play a central role in the catalytic O_2 reduction in the ubiquitously found multicopper oxidases that include tree and fungal laccases, ascorbate oxidase, ceruloplasmin, Fet3p, CueO, and CotA [1]. These enzymes contain at least four Cu centers that are necessary to catalyze the $4e^-$ reduction of O_2 to H_2O with concomitant $1e^-$ oxidations of various substrates. The electrons are taken up at the type 1 (T1) "blue" Cu site and transferred ~13 Å to the trinuclear Cu cluster site that is comprised of a type 2 (T2) "normal" and a type 3 (T3) "coupled binuclear" Cu center where the O_2 reduction occurs [2]. Reaction of the fully reduced enzyme with O_2 involves two, $2e^-$ intermediate stages [3,4]. Since the first $2e^-$ step is rate determining ($k \approx 2 \times 10^6\ M^{-1}\ s^{-1}$) [5] while the second $2e^-$ step is fast ($k > 350\ s^{-1}$) [6], the overall reaction is effectively one $4e^-$ process.

The $4e^-$ reduction of O_2 generates the native intermediate (NI), which has been trapped using a rapid freeze–quench technique and spectroscopically characterized using electron paramagnetic resonance (EPR), absorption, circular dichroism (CD), magnetic circular dichroism (MCD), and X-ray spectroscopies (XAS) [4]. It was shown that the NI is a fully oxidized species with the three Cu(II) centers in the trinuclear site mutually bridged by the product of full O_2 reduction after cleavage of the O–O bond. In particular, the study has unveiled a range of unique spectroscopic and reactivity features of the NI that originate from the all bridged structure of the trinuclear Cu cluster site. This structure promotes strong antiferromagnetic coupling of the three Cu(II) centers, yielding a doublet ground state accompanied by a low-lying doublet excited state at ~150 cm^{-1}. Accordingly, two limiting structures of the exchange coupled trinuclear Cu(II) cluster in the NI have been proposed with consideration of the enzymatic reactivity [4]: one has three μ_2-OH ligands, each bridging a Cu(II) pair, where two OH^- ligands derive from O_2 reduction and the third from ambient H_2O; the other structure has a single μ_3-oxo ligand bridging all three Cu(II) centers with the second oxygen atom from O_2 either remaining bound or dissociated from the trinuclear site.

The most characteristic spectroscopic features of the NI are, first, the absence of the T2 signal and the emergence of a broad signal with a low g_{eff} value of 1.65 in the EPR spectrum at low temperature and high radiant power, and second, the appearance of a pair of intense field- and temperature-dependent bands with opposite signs in the MCD spectrum at 316 nm (−) and 364 nm (+) that are associated with the O → Cu(II) charge transfer (CT) transitions at the trinuclear site [4]. However, the physical origins of these features have been elusive, as detailed descriptions of the electronic structure of trimeric Cu clusters have been limited.

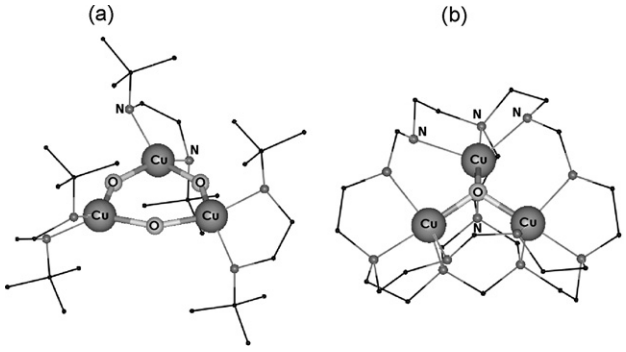

Fig. 1. Crystal structures of: (a) TrisOH and (b) μ_3O. TrisOH is D_3 symmetric with all three O-ligands in the Cu_3 plane and μ_3O is C_3 symmetric with the oxo-ligand 0.5 Å above the Cu_3 plane. N-ligand atoms are labeled for one of the three equivalent Cu centers in each structure.

In order to elucidate these unique spectral features and define the geometric and electronic structures of the NI, we have recently performed spectroscopic studies on model complexes of the tris-μ_2-hydroxy bridged and μ_3-oxo bridged trimeric Cu(II) structures, synthesized by Mirica and Stack (TrisOH, Fig. 1(a)) [7,8] and Suh et al. (μ_3O, Fig. 1(b)) [9], respectively. Compared to other relevant models available [10,11], TrisOH and μ_3O are ideal for the purpose of studying Cu–O bonds involved in the superexchange interactions and the $O^{2-}/OH^- \rightarrow$ Cu(II) CT transitions, because these have the μ_2-hydroxy/μ_3-oxo ligands as the only effective bridging ligands between the Cu centers and also lack spectroscopically non-innocent coordinating ligands or counter-anions, such as chlorides, that may dominate the UV–vis spectra.

This review presents detailed descriptions of the unique ground and excited state spectroscopic properties of the exchange coupled trigonal trimeric Cu(II) cluster in the NI building upon detailed spectroscopic and electronic structure studies of the TrisOH and μ_3O model complexes [7,12,13]. These descriptions provide further insight into the physical properties of trimeric Cu(II) complexes in general and into the reaction mechanism of the reductive cleavage of the O–O bond.

2. Ground states of exchange coupled trimeric Cu(II) clusters

2.1. Antisymmetric and anisotropic exchange

The basic description of an exchange coupled trinuclear Cu(II) complex is given by the isotropic exchange spin

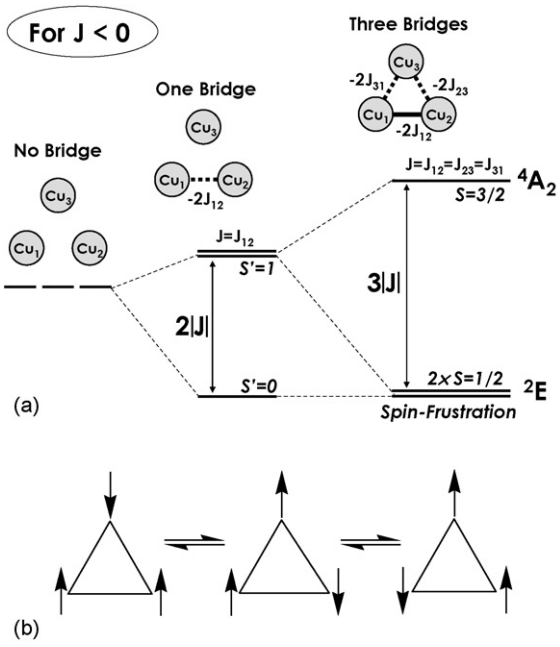

Scheme 1. (a) Energy diagram of an antiferromagnetically coupled Cu(II) trimer (all $J<0$) with zero, one, and three bridging ligands. (b) Competing spin configurations in the spin-frustrated ^{2}E ground state of a three-bridged Cu(II) trimer.

Hamiltonian from the Heisenberg, Dirac, Van Vleck (HDVV) model:

$$\hat{H}_{\text{iso}} = \sum\nolimits_{i,j} -2J(\hat{S}_i \cdot \hat{S}_j) \tag{1}$$

where $\hat{S}_i$ and $\hat{S}_j$ are local spin operators on metal centers i and j ($i, j = 1$–3, $i \neq j$) [14]. Each of the three spins can interact with its adjacent spins: the two Cu(II) centers with $S = 1/2$ couple to form intermediate spins $S' = 1$ and 0 (Scheme 1(a), 'one bridge'), which then couple to the third Cu(II) center to give $S_{\text{tot}} = 1/2$ and 3/2, and another $S_{\text{tot}} = 1/2$ state, respectively (Scheme 1(a), 'three bridges'). For the D_3/C_3 symmetric trimers with spins $S_1 = S_2 = S_3 = 1/2$ and $J = J_{12} = J_{23} = J_{31}$, the quartet and the doublet ground states are the $^4A_2/^4A$ and ^{2}E states, respectively, that are separated by $3|J|$ in energy (Scheme 1(a)).

Within the framework of the HDVV model, the two doublets in the ^{2}E state are non-interactive and the degeneracy is accidental. Thus, splitting of the two degenerate doublets is only possible via distortion of the D_3/C_3 symmetry which makes the three J's inequivalent. Static, dynamic, and magnetic Jahn–Teller effects have been proposed to account for the discrepancies from the HDVV model found in experiments [15]. However, studies on the EPR, optical, Mössbauer spectra, heat capacity, and magnetic susceptibility of various polynuclear metal clusters have demonstrated that the HDVV model is insufficient in explaining the observed data [15,16]. For example, low temperature magnetic susceptibility studies of antiferromagnetic Cu(II) trimers have reported the anomalous decline of $\chi_M T$ values below that expected for one unpaired spin system [8,17,18].

The degeneracy in the ^{2}E ground state of the three-bridged case (Scheme 1(a)) represents what is widely known as *spin frustration*. This concept is prevalent in the solid state magnetism [19–21] where it was first introduced to explain a new type of order in the spin-glasses [22,23]. In the triangular topology of the C_3/D_3 symmetric Cu(II) trimers, three spin configurations are possible, as depicted in Scheme 1(b). Here, despite all pairwise spin interactions being antiferromagnetic ($J<0$), each spin configuration comprises a pair of spins that are aligned parallel ($\uparrow\uparrow$). The term "frustration" describes a situation in which the system cannot simultaneously satisfy all of its pairwise exchange interactions and the resulting ground state can have a large degeneracy. The competing interactions of different spin configurations often lead to ground states that cannot be described in the conventional spin Hamiltonian and cause a dramatic modification of the magnetic properties.

Various studies have demonstrated that the spin frustration in the ground states of antiferromagnetically coupled metal complexes must be lifted via higher-order exchange terms such as antisymmetric (=Dzialoshinsky–Moriya) [24,25], anisotropic (=pseudo-dipolar), or biquadratic exchange effects [15,16]. In particular, the antisymmetric and anisotropic exchange effects are first- and second-order in spin–orbit coupling (SOC) in an exchange coupled system and have been suggested to be the two largest non-Heisenberg term available, especially for trinuclear systems [16]. These terms are introduced into the spin Hamiltonian by treating the interaction between a pair of spins with a second rank tensor that can be decomposed into the sum of a symmetric and a traceless antisymmetric tensor [26]. The former can be further divided into a diagonal and a traceless symmetric tensor. Consequently, the spin Hamiltonian for the two center interactions can be written as:

$$\hat{H}_{12} = -2J\hat{S}_1 \cdot \hat{S}_2 + \hat{S}_1 \cdot D \cdot \hat{S}_2 + \vec{G}(\hat{S}_1 \times \hat{S}_2) \tag{2}$$

where the first term is the isotropic, the second is the aniostropic exchange, and the third is the antisymmetric exchange ($\vec{d}$ is also often used in the literature instead of $\vec{G}$) terms. Note that the isotropic or aniostropic exchange terms tend to orient the spins parallel or antiparallel to each other, while the antisymmetric exchange term induces spin-canting to minimize the interaction energies. The aniostropic and antisymmetric exchange terms, described purely by the off-diagonal matrix elements, become consequential when the zeroth-order magnetic orbitals are modulated by perturbations such as SOC.

Physical descriptions and quantitative expressions of the antisymmetric and anisotropic exchange contributions have been provided, first by Moriya [24], to explain the weak ferromagnetism in antiferromagnetic crystals such as α-Fe_2O_3 and NiF_2, and later by Kanamori [27], who gave more explicit descriptions of the superexchange between the ground state of one metal center to the excited state of the other metal center. From perturbation theory, these are expressed as:

$$G_{12} = 2i\lambda \left[\frac{\langle e_1|L_1|g_1\rangle}{\Delta_1}(-2J^{e_1 g_2}_{g_1 g_2}) - \frac{\langle e_2|L_2|g_2\rangle}{\Delta_2}(-2J^{g_1 e_2}_{g_1 g_2}) \right] \tag{3}$$

$$D_{12} = \lambda^2 \left[\frac{\langle e_1|L_1|g_1\rangle^2}{\Delta_1^2}(-2J_{e_1g_2}^{e_1g_2}) + \frac{\langle e_2|L_2|g_2\rangle^2}{\Delta_2^2}(-2J_{g_1e_2}^{g_1e_2}) \right] \quad (4)$$

where λ is the SOC parameter, $|g_i\rangle$ and $|e_i\rangle$ the ground and excited states at the ith metal center, Δ_i the energy difference between $|g_i\rangle$ and $|e_i\rangle$, L_i the orbital angular momentum operator that couples $|g_i\rangle$ and $|e_i\rangle$, and $J_{e_1g_2}^{e_1g_2} = \langle\phi_e^1(1)\phi_g^2(2)|\hat{H}_{ex}|\phi_e^1(2)\phi_g^2(1)\rangle$ is the transfer integral (equivalent definitions for $J_{g_1g_2}^{e_1g_2}$, $J_{g_1e_2}^{g_1e_2}$, and $J_{g_1e_2}^{g_1e_2}$), where ϕ_g and ϕ_e are the ground and excited wave functions at each metal center indicated by superscripts 1 and 2, while 1 and 2 in parentheses refer to electrons; the exchange Hamiltonian $\hat{H}_{ex}$ in the transfer integral expression includes contributions from both the two electron Coulomb operator $1/r_{12}$ and the superexchange derived from metal–ligand overlap. Thus, $J_{g_1g_2}^{e_1g_2}$ involves exchange coupling of one electron in the ground state of metal 1 to the ground state of metal 2 and the second electron from the ground state of metal 2 to the excited state of metal 1, while $J_{e_1g_2}^{e_1g_2}$ involves exchange of both electrons between the excited state of metal 1 and the ground state of metal 2.

As indicated by Eqs. (3) and (4), the antisymmetric and anisotropic exchanges are the first- and second-order SOC effects, with magnitudes approximated by $(\Delta g/g)|2J|$ and $(\Delta g/g)^2|2J|$, respectively, where Δg is the deviation of g from the free electron $g_e = 2.0023$. It is important to note that both are derived from the synergistic effects of single-centered SOC and superexchange interactions between the ground state of one center to the excited state of the other center, and vice versa. However, the antisymmetric exchange follows a set of symmetry rules and vanishes when, for example, the metal centers are symmetrically related by a center of inversion [24]. The anisotropic exchange, on the other hand, is not limited by such rules and is present in complexes of all symmetry. Consequently, it is often the case that only the anisotropic exchange is considered in dimeric Cu(II) complexes. In trigonal trimeric complexes, the lack of a center of inversion allows a non-zero component of the antisymmetric exchange to be present in the direction normal to the metal plane. Indeed, it has been suggested that the antisymmetric exchange is the largest non-HDVV term available to account for the zero-field splitting (ZFS) in the antiferromagnetic ^{2}E ground state of a trimeric Cu(II) complex; in the ferromagnetically coupled $^4A_2/^4A$ state (Scheme 1(a)), the largest term is the anisotropic exchange due to the absence of orbital degeneracy/orbital angular momentum.

It should be noted that another, but obvious, source of ZFS in the $^4A_2/^4A$ and ^{2}E states of trimeric Cu(II) complexes is the magnetic spin–spin dipolar interaction that derives from the mutual influence of the magnetic field created by the magnetic centers on each other [28]. Its magnitude can be estimated using a point dipole model with $|D_{dd}| \approx 0.65 g_\parallel^2/r^3$, in which r is in Å [29]. This model estimates $|D_{dd}|$ of 0.22 and 0.27 cm^{-1} for TrisOH ($g_\parallel = 2.32$ and $r = 3.64$ Å) and μ_3O ($g_\parallel = 2.064$ and $r = 3.105/3.125$ Å), respectively. However, TrisOH and μ_3O show ZFS of 65.0 cm^{-1} [7] and 5.0 cm^{-1} [13] in their ^{2}E and ^{4}A ground states, respectively, suggesting that the magnetic spin–spin dipolar contribution to the ZFS is minor.

2.2. Antisymmetric exchange in the spin frustrated ^2E ground state of TrisOH

The spin frustrated ^{2}E ground state of a Cu(II) trimer can be best illustrated by TrisOH (Fig. 1(a)). The structure of TrisOH has been determined by X-ray crystallography at −130 °C to have rigorous D_3 symmetry. As the closest distance between metal sites of different trimer molecules is 9.2 Å, the effect of intermolecular magnetic interaction is negligible. The magnetic susceptibility data from 80 to 290 K yield an isotropic exchange constant J of −105 cm^{-1} and thus, $3|J| = 315$ cm^{-1} as the molecular doublet–quartet splitting energy. At lower temperatures, however, the magnetization decreases well below and then increases above that of an isolated $S = 1/2$ spin system [8]. This phenomenon has been reported for other Cu(II) trimers and necessitated the incorporation of the antisymmetric exchange term in the simulations of these magnetization curves [17,18].

Considerable progress has been made in the theoretical predictions of the behavior of the ^{2}E ground state of trinuclear Cu(II) clusters, by Tsukerblat et al. in particular [16,30]. In their treatment of trigonal trimeric Cu(II) systems, a spin Hamiltonian that accounts for the antisymmetric exchange and differences in the three isotropic exchanges is implemented (note that anisotropic exchange is not present in an $S = 1/2$ system [16]). With consideration of the Zeeman splitting in applied magnetic field B, the spin Hamiltonian is written as:

$$\begin{aligned}\hat{H} = {} & -2J(\hat{S}_1 \cdot \hat{S}_2 + \hat{S}_2 \cdot \hat{S}_3 + \hat{S}_1 \cdot \hat{S}_3) + \delta(\hat{S}_1 \cdot \hat{S}_2) \\ & + \delta'(\hat{S}_1 \cdot \hat{S}_3) + \vec{G} \cdot ([\hat{S}_1 \times \hat{S}_2] + [\hat{S}_2 \times \hat{S}_3] + [\hat{S}_3 \times \hat{S}_1]) \\ & + (g_z \cos\theta + g_{xy} \sin\theta)\beta B(\hat{S}_1 + \hat{S}_2 + \hat{S}_3) \end{aligned} \quad (5)$$

where δ and δ' are the changes in the isotropic exchange ($\delta = J_{12} - J_{23}$ and $\delta' = J_{13} - J_{23}$) due to symmetry lowering and θ is the angle between the applied magnetic field and the z-axis of the molecule (i.e. the C_3-axis normal to the Cu_3 plane). The vector components of the antisymmetric exchange follow the relation $G_z \gg (G_x, G_y) \approx 0$, which can be derived from the symmetry properties of the $\vec{G}$ vector [24].

The above spin Hamiltonian operates on a set of four spin basis functions $|S', S, M_S\rangle = |0, 1/2, \pm 1/2\rangle$ and $|1, 1/2, \pm 1/2\rangle$. The eigenvalues and eigenfunctions obtained describe the ZFS and the extent of mixing between the two doublets as functions of the antisymmetric exchange G (=G_z) and the symmetry lowering δ. The ZFS (Δ, Scheme 2) of the ^{2}E ground state is expressed as:

$$\Delta = \sqrt{\delta^2 + 3G^2} \quad (6)$$

If only the symmetry distortion is present ($G = 0$, $\delta \neq 0$), Δ equals δ, and the eigenfunctions are functions of either $|0, 1/2, \pm 1/2\rangle$ or $|1, 1/2, \pm 1/2\rangle$ which suggests localization of the spin density on individual metal centers. In such a case, the two degenerate doublets of the ^{2}E ground state split in energy due to the differences in isotropic exchange coupling constants

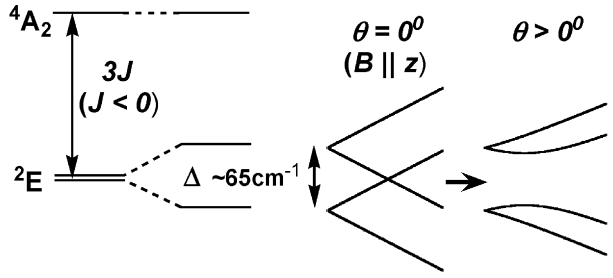

Scheme 2.

($J_{12} \neq J_{23} \neq J_{31}$). These doublets are non-interactive as the splitting is not caused by SOC (i.e. no off-diagonal matrix elements that allow spin–orbit mixing of the doublet states). Alternatively, if there is only the antisymmetric exchange present ($G \neq 0$, $\delta = 0$), Δ equals $\sqrt{3}G$, and the eigenfunctions become complex combinations of the spin basis functions as $(1/\sqrt{2})|0,1/2, \pm 1/2\rangle \pm i(1/\sqrt{2})|1, 1/2, \pm 1/2\rangle$, where $i = \sqrt{-1}$. The spin densities are now delocalized and equally distributed over the three metal centers. The antisymmetric exchange acts to mix the two zero-field split doublets of the ^{2}E ground state, which becomes evident when a magnetic field is applied to the system.

Direct experimental evidence for the ZFS in the ^{2}E ground state of a Cu(II) trimer that are associated with the combined effects of the antisymmetric exchange and symmetric lowering has been obtained from TrisOH [7]. First, the field- and temperature-dependent MCD intensity (i.e. MCD *C*-term; see Section 3) allows observation of a low-lying excited doublet that is a zero-field split component of the ^{2}E ground state of the trimer. In the Curie plot of the MCD intensity that is associated with an *x*,*y*-polarized $OH^- \rightarrow$ Cu(II) CT transition, deviation from the linear dependence on $1/T$ at a fixed non-saturating magnetic field is observed at $T > 30$ K (Fig. 2). Likewise, a

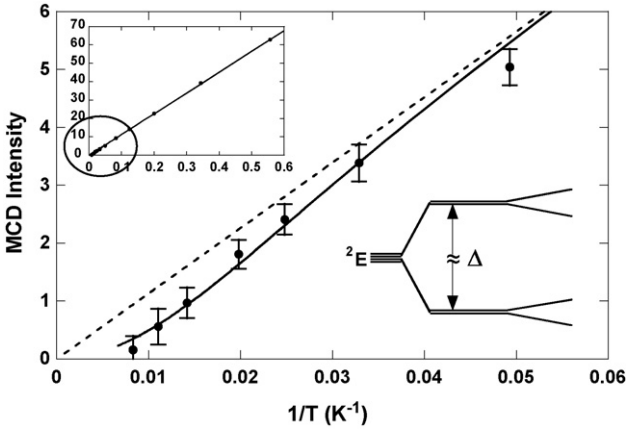

Fig. 2. $1/T$ Curie plot of the MCD intensity at 330 nm (band 9 in Fig. 10) at a fixed magnetic field of 0.7 T. Data points were collected over 12 temperatures between 1.78 and 120 K. The main panel shows data points between 20 and 120 K, which is the expanded view of the circled region in the inset. The simulation assumed two level Boltzmann distribution with each state having MCD *C*-terms with the same magnitude but with opposite signs (solid line). The linear $1/T$ dependence of one-level systems (i.e. infinite Δ limit in the two level systems) is shown in the dotted line for comparison (reproduced with permission from ref. [7], ©2004 American Chemical Society).

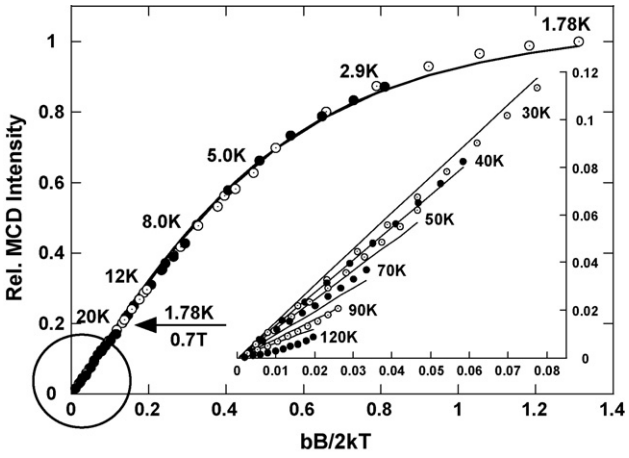

Fig. 3. Variable-temperature variable-field MCD (VTVH MCD) saturation plot of TrisOH (mull) at 330 nm. Twelve isotherms are shown with normalized intensities. Simulations were performed with two $S = 1/2$ Kramers doublets, both with $g_z = 2.32$, $g_{x,y}$ (effective) = 0, and equal *C*-term intensities (A_{satlim}) but with opposite signs. Contributions from MCD *A*- and *B*-terms were ignored. Splitting between the two doublets, i.e. $\Delta = 65.0$ cm^{-1}, is obtained. The arrow indicates 0.7 T in the 1.78 K isotherm (see Fig. 2) (reproduced with permission from ref. [7], ©2004 American Chemical Society).

variable-temperature variable-field MCD (VTVH MCD) saturation plot of the same transition shows no nesting behavior (i.e. lack of overlap between the saturation curves obtained at different temperatures) at low temperatures, while a distinct nesting behavior is observed at $T > 30$ K where an increase in temperature causes reduction of the relative MCD intensity and a gradual decrease of the slope of the isotherms (Fig. 3).

These anomalous behaviors of the $S_{tot} = 1/2$ ground state of TrisOH are indicative of ZFS of the ^{2}E ground state. As the two zero-field split doublets of the ^{2}E ground state have orbital angular momenta of opposite signs ($L_z = \pm 1$), the field- and temperature-dependent MCD intensity (i.e. MCD *C*-term; see Section 3) from the low-lying excited doublet (i.e. the higher energy component of the zero-field split ^{2}E ground state) would have an opposite sign to that of the ground doublet, resulting in cancelation of the intensity of the latter at high temperature where Boltzmann population of the low-lying excited doublet would occur. With consideration of two-state Boltzmann distribution, the ZFS is determined to be ~65 cm^{-1} from simulations of both the Curie and VTVH MCD plots (Figs. 2 and 3). If we neglect the effect of symmetry lowering ($\delta = 0$), which would be the case for a rigorous D_3/C_3 structure, the antisymmetric exchange G ($=G_z$) in the ^{2}E ground state of TrisOH would be 37.5 cm^{-1} (i.e. $\Delta = \sqrt{3}G$).

The powder EPR spectrum of TrisOH is presented in Fig. 4, with a transition at $g = 2.32$. Since the ZFS of 65 cm^{-1} is much larger than the microwave energy at X- or Q-band, the observed transition occurs within the Zeeman split subcomponents of the ground doublet at low temperatures. It is important to note that when the molecular C_3-axis is aligned with the applied magnetic field ($\theta = 0°$), the transition probability is given by:

$$|\langle \Psi^+_{lower}|\hat{S}_+ + \hat{S}_-|\Psi^-_{lower}\rangle|^2 \propto \frac{\delta^2}{\Delta^2} \quad (7)$$

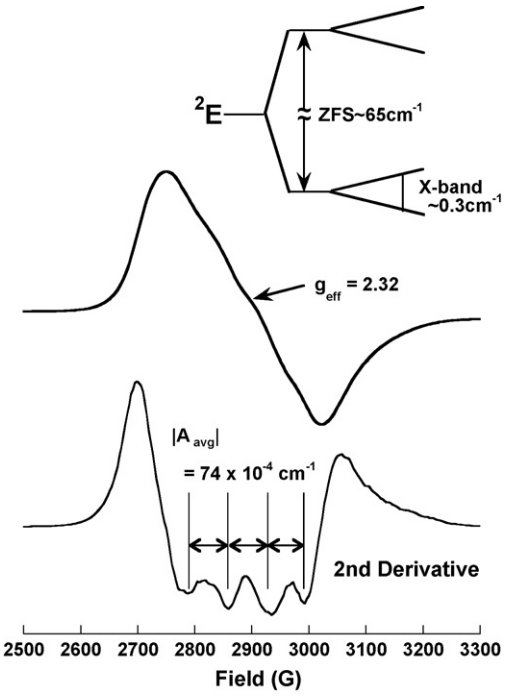

Fig. 4. X-band EPR spectrum of powder TrisOH sample at 5 K, 9.39 GHz (top) and second derivative plot of the EPR spectrum (bottom). Four-line hyperfine splitting pattern is indicated (reproduced with permission from ref. [7], © 2004 American Chemical Society).

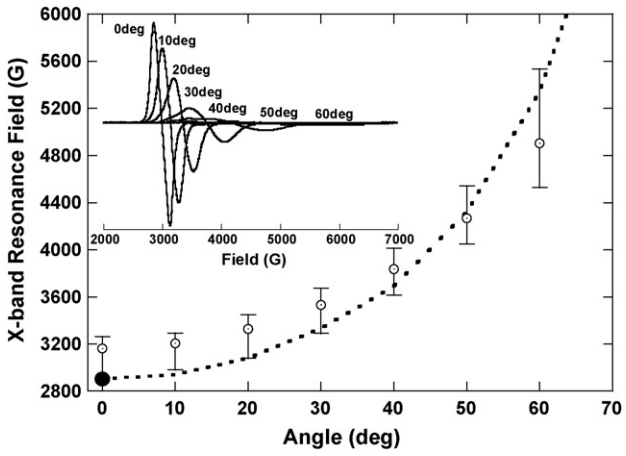

Fig. 5. Resonance fields of the single crystal TrisOH in X-band EPR. The horizontal axis of the plot defines the angle between the molecular z-axis (the C_3-axis normal to the Cu_3 plane) relative to the applied magnetic field. Each point gives the average of five experiments (in open circles) and the high/low values (error bars). The resonance field of the powder EPR spectrum is indicated by the filled circle at 0°. Fits were made by varying the antisymmetric exchange (G) and distortion factor (δ). The dotted curve represents the simulated angular dependence of the EPR transitions with the best fit values. (Inset) The overlay of the actual single crystal EPR spectra at various angles (reproduced with permission from ref. [7], ©2004 American Chemical Society).

where Ψ^{+}_{lower} and Ψ^{-}_{lower} are the wave functions of the Zeeman levels of the ground doublet. This indicates that the observed transition is allowed only if the symmetry is lowered ($\delta \neq 0$) in the TrisOH structure, at least at $T < 30$ K where the EPR transitions are observed. The possibility of a magnetic Jahn–Teller effect in the ^{2}E ground state of antiferromagnetic trinuclear complex to remove the three-fold symmetry has been proposed, suggesting a distortion of ~0.01 Å [31]. Recently, Cage et al. attributed the symmetry lowering they observed to such a magnetic Jahn–Teller effect [32]. For TrisOH, the crystallographic D_3 symmetry reflects either a dynamic or a static Jahn–Teller distortion where the latter would be distributed over the three orientations. However, the low Jahn–Teller stabilization energy (~4–5 cm^{-1}) and small structural distortion (~0.01 Å) make it difficult to distinguish these effects through crystallography even at very low temperature.

The most dramatic spectroscopic evidence for the antisymmetric exchange in TrisOH is the strong anisotropy observed in the single crystal EPR spectrum in which the g_{eff} value spans a range of 2.32 down to an unprecedented 1.2; g_{eff} values lower than 1.2 were not detected due to signal broadening and the detection limit of the EPR instrument (Fig. 5). When $\theta = 0°$, the applied magnetic field aligns the spins with G_z and this results in energy levels that are linear superpositions of the orbital angular momentum provided by the antisymmetric exchange and the spin angular momenta of the individual metal centers. The two zero-field split doublets split linearly with applied magnetic field, with the monomeric g_z value of a Cu(II) center in the trimer. However, when $\theta \neq 0°$, the spins are no longer aligned with G_z by the applied magnetic field and this causes the two doublets to undergo field-induced mixing that results in a non-linear splitting with applied magnetic field (Scheme 2, $\theta > 0°$). Consequently, the resonances with fixed X-/Q-band radiation energies are shifted to higher field positions that yield the observed low g_{eff} values. A best fit, using Eq. (6) and $\Delta = 65.0$ cm^{-1}, has been obtained with $G = 36.0$ cm^{-1} and $\delta = 17.5$ cm^{-1}. The G obtained is only ~1.5 cm^{-1} different from the value obtained for the $\delta = 0$ case, suggesting that when G is large, it is not very sensitive to δ.

Given the experimental values of Δ, G, and δ, a quantitative description of the ground state spin wave functions is accessible. In particular, it can be readily shown that in the isosceles distortion limit ($\delta = \delta'$ in Eq. (5)), the spin density is distributed 42, 29, and 29% over the three Cu(II) centers in the doublet ground state and 24, 38, and 38% in the low-lying doublet excited state, all deviating from the spin density of 33% in a totally delocalized trimeric system (Scheme 3). The hyperfine splittings in the powder X-band EPR spectrum (Fig. 4) would arise from the combined contributions from all of the metal sites. Each of the four hyperfine lines from the unique Cu(II) center (with

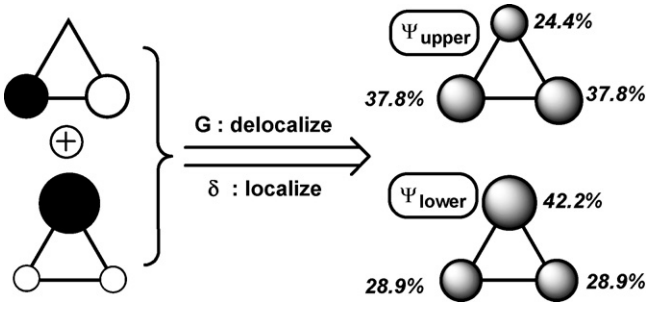

Scheme 3. Reproduced with permission from ref. [7], ©2004 American Chemical Society.

42% spin density in the ground doublet state) would further split into 7 hyperfine lines (28 total) with relative intensities of 1:2:3:4:3:2:1 that derive from the other two Cu(II) centers (with 29% spin density each). From the simulation, the positions of the four minima in the second derivative plot in Fig. 4(bottom) are very similar to the positions of four hyperfine lines of the unique metal center; the small shifts in positions are caused by the contributions from superposition of the other metal hyperfine lines. Thus, it can be estimated that the observed hyperfine splitting, $|A_{avg}| = 74 \times 10^{-4}\,cm^{-1}$, is about 42% of the $|A_{\|}|$ value of an isolated Cu(II) site. Scaling up the observed value by 2.4 (=1/42%) yields $180 \times 10^{-4}\,cm^{-1}$, which is a reasonable value for a typical Cu(II) parallel hyperfine splitting. Thus, the competing effects of delocalization by the antisymmetric exchange and localization by the symmetry lowering result in a significant reduction of the observed parallel hyperfine splitting.

Finally, the orbital origin of the large antisymmetric exchange interaction of $\sim 36\,cm^{-1}$ can be found by evaluating the specific SOC pathways between each pair of metal centers. As indicated above, the combined effects of the local SOC, ground-to-ground, and ground-to-excited state superexchange interactions are required for the antisymmetric exchange. As obtained by density functional theory (DFT) calculations, the $d_{x^2-y^2}$ orbital ground state on a metal site in TrisOH can spin–orbit couple with the d_{xy} excited state on the same site via L_z. Further, the Cu–O–Cu angle of 144.2° provides both the ground-to-ground ($d_{x^2-y^2}/d_{x^2-y^2}$) as well as the ground-to-excited ($d_{x^2-y^2}/d_{xy}$) superexchange pathways via Cu–O σ-bonds (Scheme 4). These lead to the large values of $J^{e_1g_2}_{g_1g_2}$ and $J^{g_1e_2}_{g_1g_2}$ integrals for the antisymmetric exchange in Eq. (3).

Comparison with the trimeric Cu(II) complex by Cage et al. [32] exemplifies the importance of the superexchange between the ground $d_{x^2-y^2}$-orbitals and the excited d_{xy}-orbitals. In this structure, the *x*,*y*-plane of each metal site is perpendicular to the Cu_3 plane. Consequently, the $d_{x^2-y^2}$- and d_{xy}-orbitals are orthogonal and have poor ground-to-excited state superexchange interactions, leading to weak antisymmetric exchange. Analysis of the EPR data on this complex only required consideration of the symmetry lowering effect, implying that the antisymmetric exchange is small. On the other hand, the ground-to-ground $d_{x^2-y^2}/d_{x^2-y^2}$-orbital pairs form good superexchange pathways through σ-type bonds facilitated by two bridging carboxylate ligands between each metal pair, resulting in an antiferromagnetic ground state with $J \sim -107\,cm^{-1}$. This illustrates that the

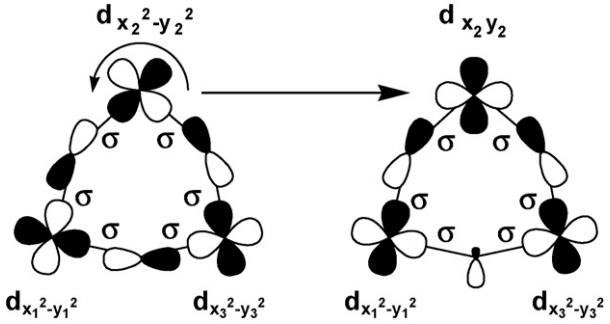

Scheme 4.

estimation of the *G*-value by the relation $\propto (\Delta g/g)|2J|$ can be misleading, as the *J* in this formulation is just the ground state isotropic exchange parameter. Similar arguments can be formulated for the anisotropic exchange interactions in dimeric Cu(II) complexes [33,34]. For example, the experimental determination of excited state exchange coupling parameters in dimeric Cu acetate pyrazine has clearly demonstrated that the different exchange pathways would have distinctly different contributions to the total anisotropic exchange, and thus, to the ZFS of the triplet ground state of the dimer [33].

2.3. Anisotropic exchange in the ^4A ground state of μ_3O

The properties of the ^4A ground state are best exemplified by μ_3O, which is a C_3 symmetric Cu(II) trimer with quartet–doublet energy splitting ($3|J|$) of $163.5\,cm^{-1}$ as determined by magnetic susceptibility [9]. This model complex is the only μ_3-oxo bridged trimeric Cu(II) complex without other effective bridging ligands, such as pyrazolates [11], that may significantly affect the exchange coupling. The distances between the Cu centers of the two neighboring trimer units are large enough (closest = 9.67 Å) to avoid significant intermolecular interactions. Moreover, μ_3O exists in a protonated form, μ_3OH ($pK_a \sim 4.6$ in aq.), that has been also determined to be C_3 symmetric. Thus, the bonding interactions between the μ_3-oxo ligand and the Cu(II) centers can be greatly simplified, while the protonated μ_3OH form can be used as a perturbation to the Cu–O bonding interactions in μ_3O.

The powder EPR spectra of μ_3O taken at X- and Q-bands are presented in Fig. 6 [13]. The EPR signals are observed only below 120 K and their intensities reach their maxima near 8 K. Two transitions are observed at g_{eff} of 3.64 and 2.06 in X-band and 3.77 and 2.06 in Q-band. These transitions correspond to the resonances at $g = 4$ and 2 that reflect transitions within the $M_S = \pm 1/2$ component of a zero-field split axial $S_{tot} = 3/2$ system (Scheme 5). However, the g_{eff} of 3.64/3.77 (X-/Q-band) is lower than 4.0, which would correspond to a true $g_{x,y}$ of 1.82/1.89 that is too low for the individual Cu centers in μ_3O. Note that low g_{eff} values are also observed when the oxo-bridge is protonated (Fig. 7) with g_{eff} of 3.70 and 2.22. Moreover, the Q-band spectrum (Fig. 7(b)) shows an additional transition at $g_{eff} \sim 5.57$ that corresponds to the $\Delta M = \pm 2$ transition between the $M_S = \pm 1/2$ and $\pm 3/2$ doublets of the zero-field split ^4A ground state.

The observed low g_{eff} values for μ_3O and μ_3OH originate from the mixing of the upper ($M_S = \pm 1/2$) and lower ($M_S = \pm 3/2$) doublets of the zero-field split ^4A ground state. As a result, the Zeeman levels become non-linear when the molecular *z*-axis is not aligned with the magnetic field. Thus, the low g_{eff} value (<4.0) reflects an EPR transition between the perturbed and non-linear $M_S = \pm 1/2$ Zeeman levels. In addition, the $\Delta M = \pm 2$ transition at $g_{eff} \sim 5.57$ observed in the Q-band spectrum (but not in X-band) of μ_3OH indicates that the ZFS is comparable to the Q-band energy and that the $M_S = \pm 1/2$ doublet is considerably mixed into the $M_S = \pm 3/2$ state such that EPR transition between the two doublet states becomes partially allowed.

The SOC that results in ZFS and mixing of the doublet components in the ^4A ground state is governed by the anisotropic

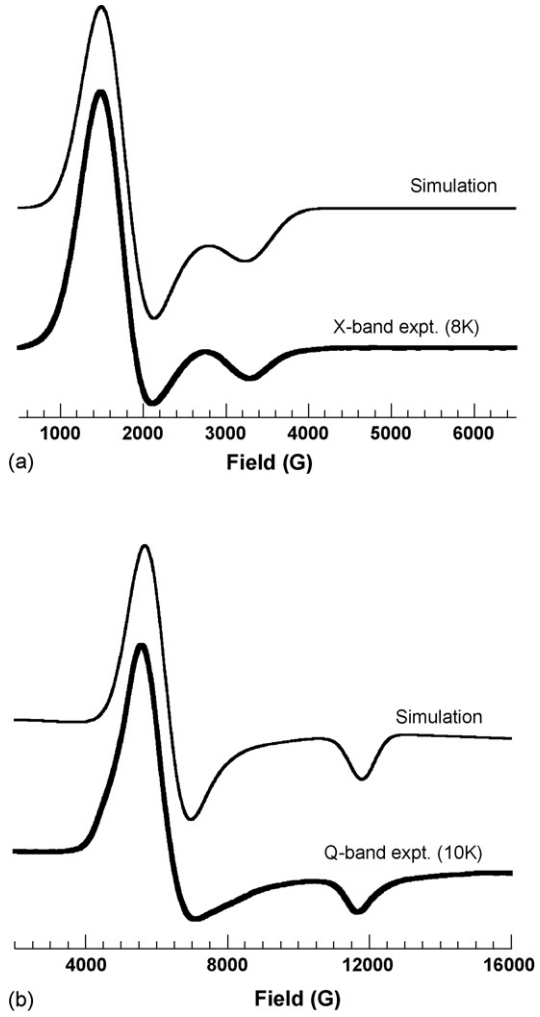

Fig. 6. EPR spectra of powder μ_3O complex and their simulations using $g_x = g_y = 2.021$, $g_z = 2.064$, $D = -2.50\,cm^{-1}$, $E/D = 0$, line width parameters $W_{x,y,z} = (650, 650, 280\,G)$, and the ZFS D–E strain parameters σ_D and $\sigma_E = 0.06$ and 0.07, respectively. (a) X-band spectrum taken at 0.3 mW, 8.0 K, and 9.390 GHz and (b) Q-band EPR spectrum at 0.097 mW, 10.0 K, and 33.81 GHz (reproduced with permission from ref. [13], ©2005 American Chemical Society).

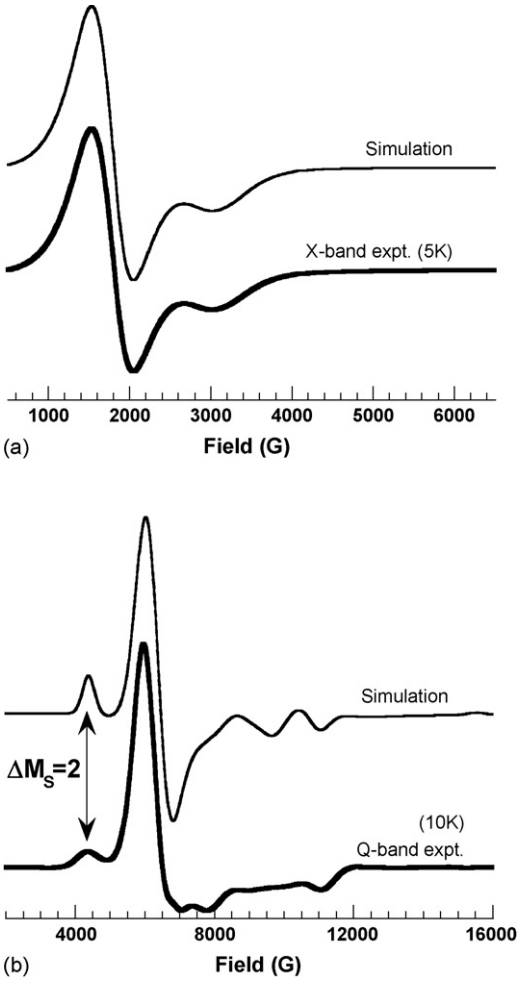

Fig. 7. EPR spectra of powder μ_3OH complex and their simulations using $g_x = g_y = 2.067$, $g_z = 2.224$, $D = -1.02\,cm^{-1}$, $E/D = 0$, line width parameters $W_{x,y,z} = (580, 580, 330\,G)$, and the ZFS D–E strain parameters σ_D and $\sigma_E = 0.05$ and 0.03, respectively. (a) X-band spectrum taken at 0.3 mW, 7.6 K, and 9.390 GHz and (b) Q-band EPR spectrum at 0.097 mW, 10.0 K, and 33.95 GHz (reproduced with permission from ref. [13], ©2005 American Chemical Society).

exchange (Eq. (4)). Due to the lack of orbital angular momentum, the ZFS of 2D in a ^{4}A state would be second-order in SOC and its effect is significantly smaller than that of the first-order antisymmetric exchange in a ^{2}E state (see above). Nevertheless, the anisotropic exchange shares the same physical origin as the antisymmetric exchange (Eq. (3)); i.e. it derives from local SOC and ground-to-excited state superexchange interactions. As obtained by DFT calculations, the d_{z^2} ground state in μ_3O undergoes SOC with the d_{xz} excited state via L_y (∼molecular L_z, since local y-axis ∼ molecular z-axis) at each metal center. Further, the ground-to-excited state superexchange between d_{z^2}- and d_{xz}-orbitals of different metal centers is facilitated via the in-plane oxo p-orbitals (Scheme 6). Thus, the ZFS of $-5.0\,cm^{-1}$ in the ^{4}A ground state in μ_3O provides experimental evidence, in magnitude and sign, for the existence of the anisotropic exchange and the contribution of the local SOC and ground-to-excited state superexchange.

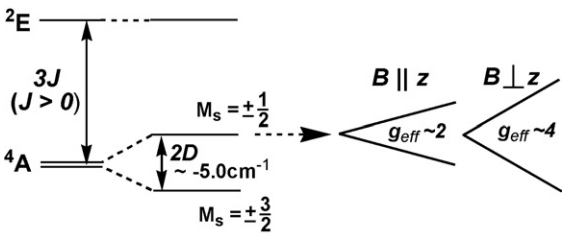

Scheme 5. Reproduced with permission from ref. [13], ©2005 American Chemical Society.

Note that the ferromagnetic ground state of μ_3O is not intrinsic to the μ_3-oxo bridged structure, but derives from the oxo-ligand being out of the Cu_3 plane by ∼0.5 Å, likely due to the rigid macrocyclic ligand. However, it can attain an antiferromagnetic ^{2}E ground state when the oxo-ligand is brought closer to the Cu_3 plane, as indicated by DFT calculations [13]. When the oxo-ligand is out of the plane, the Cu d_{z^2}-O p_z bonding interactions

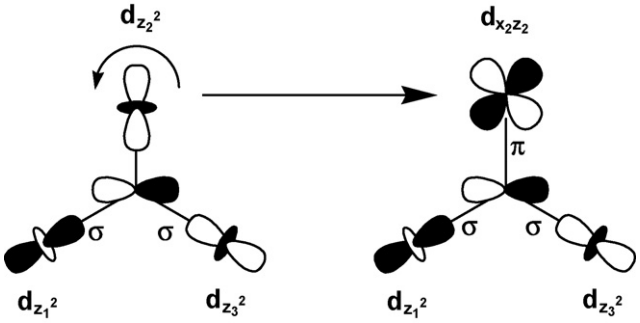

Scheme 6. Reproduced with permission from ref. [13], ©2005 American Chemical Society.

become substantial in the singly occupied MO (SOMO with a^* symmetry; Scheme 7, left). The resulting pseudo-σ-bonds destabilize the SOMO and decrease its energy gap with the SOMO + 1 (e^* symmetry MO with in-plane oxo p_x- and p_y-orbital character mixed into the d-orbitals). Consequently, the ferromagnetic contribution in the exchange interaction dominates over the antiferromagnetic contribution, as described by the magnetic theory of Hay et al. [35]. In contrast, if the oxo-ligand is in the Cu_3 plane, the Cu–O pseudo-σ-bonds are lost and the SOMO energy is stabilized, increasing the SOMO/SOMO + 1 energy gap. As a result, the antiferromagnetic contribution, being proportional to the square of the SOMO/SOMO + 1 energy gap [35], dominates over the ferromagnetic contribution (∼constant), yielding a ^{2}E ground state (Scheme 7, right).

The experimental evidence for the anisotropic exchange in the ferromagnetic ^{4}A ground state of μ_3O allows us to anticipate a large ZFS in the ^{2}E ground state of an antiferromagnetically coupled μ_3O by the antisymmetric exchange as the antisymmetric and anisotropic exchanges share the same physical origin. In the μ_3O structure, the ground-to-excited exchange ($J^{e_1g_2}_{e_1g_2} = J^{xz_1z_2^2}_{z_1^2z_2^2}$ in Eq. (4)) should be larger than the ground-to-ground exchange as the ground-to-excited antiferromagnetic coupling is further facilitated by the π-bond between d_{xz} and the in-plane oxo p-orbital which also interacts with d_{z^2} on the adjacent Cu centers via σ-bonds (Scheme 6). Using the calculated ground state exchange coupling constant J of $-55.2\,cm^{-1}$ when the oxo-ligand is in the Cu_3 plane as a lower limit for $J^{xz_1z_2^2}_{z_1^2z_2^2}$, the magnitude of the pairwise antisymmetric exchange parameter G (=G_z) of $42\,cm^{-1}$ is estimated [13]. Accordingly, the ^{2}E ground state of μ_3O would exhibit a ZFS of $\sim 70\,cm^{-1}$ ($\Delta = \sqrt{3}G$) from the antisymmetric exchange. Consequently, an antiferromagnetically coupled μ_3O is also expected to produce EPR signals with low g_{eff} values at perpendicular field orientation as the antisymmetric exchange facilitates spin–orbit mixing of the zero-field split doublets of the ^{2}E ground state (Scheme 2, right).

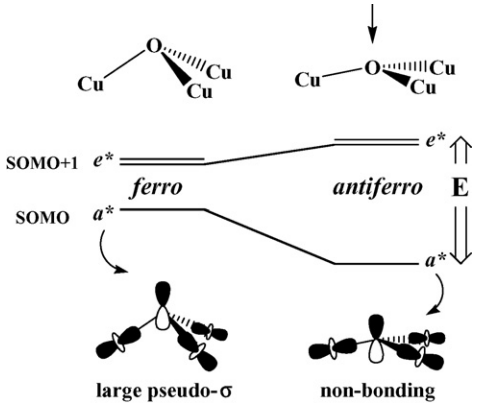

Scheme 7. Reproduced with permission from ref. [13], ©2005 American Chemical Society.

2.4. Ground state of the native intermediate

Fig. 8 presents the EPR spectrum of the *Rhus vernicifera* tree laccase in the two of its fully oxidized forms, namely the resting oxidized and the NI. In the resting oxidized form, two of the four Cu(II) centers are paramagnetic, which are observed as the T1 and T2 signals (Fig. 8(a)). The T1 "blue" Cu signal exhibits $g_\parallel$ value at 2.30 and the characteristic small hyperfine splitting $A_\parallel$ of $39 \times 10^{-4}\,cm^{-1}$, consistent with the $d_{x^2-y^2}$ ground state of its trigonal pyramidal ligand environment with two histidines and a cysteine in the *x*,*y*-plane (Scheme 8, T1). In particular, the small hyperfine splitting originates from the highly covalent Cu–S bond, as has been demonstrated by single crystal EPR and XAS edge studies on various blue Cu proteins [36,37]. The T2 "normal" Cu EPR signal exhibits $g_\parallel$ value at 2.24 and hyperfine splitting $A_\parallel$ of $180 \times 10^{-4}\,cm^{-1}$, consistent with the $d_{x^2-y^2}$ ground state in its T-shaped ligand environment with two histidines and a hydroxide in the *x*,*y*-plane (Scheme 8, T2) [38]. This T2 Cu is coordinatively unsaturated; there is an open site oriented towards the center of the trinuclear Cu cluster as demonstrated by various crystallographic [39], spectroscopic, and computational studies, as well as exogenous ligand binding studies [38]. The other two Cu(II) centers in the trinuclear Cu cluster make up the T3 "coupled-binuclear" site that are antiferromagnetically coupled via a OH^- bridge (Scheme 8, T3) and thus, do not show up in the EPR spectrum. In the resting oxidized form, the T2 and T3 Cu centers have no direct bridging ligand and the two sites have negligible magnetic influence on each other.

In contrast to the resting oxidized form, the EPR spectrum of the NI form at 77 K exhibits only the T1 signal; the signal related

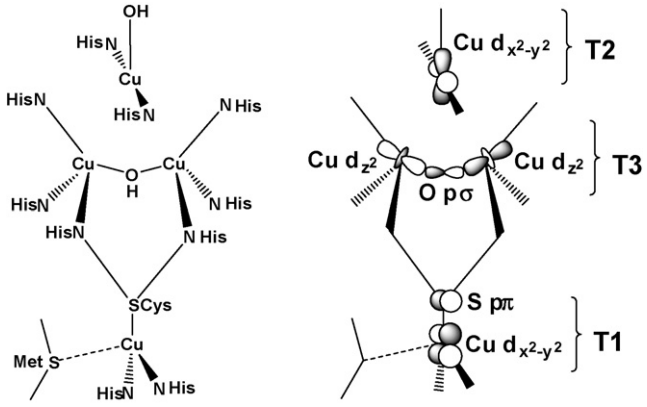

Scheme 8.

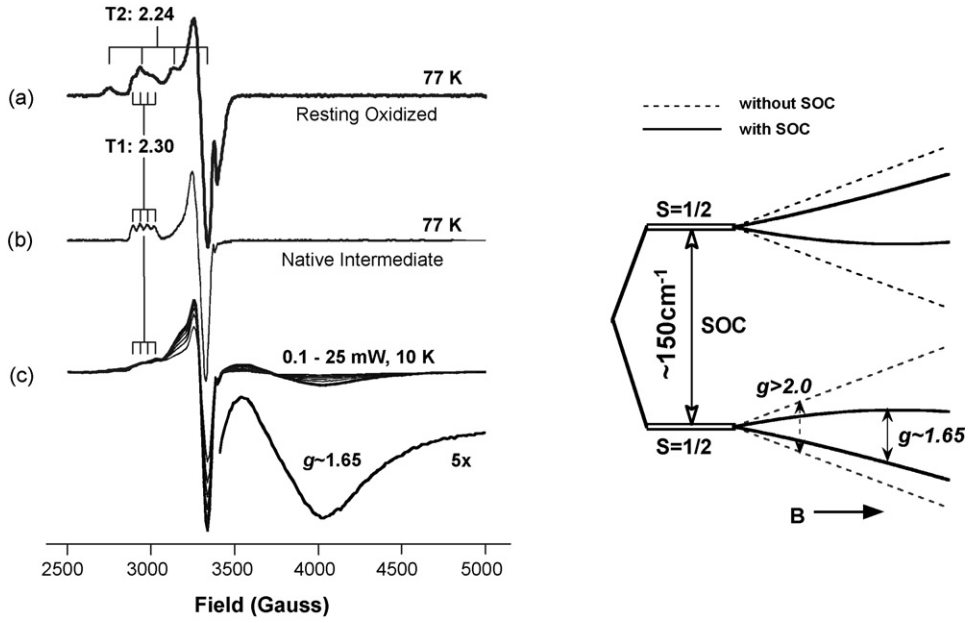

Fig. 8. X-band EPR spectra of the *Rhus vernicifera* tree laccase: (a) the resting oxidized form at 2.02 mW and 77 K, in which both the type 1 (T1) and type 2 (T2) Cu EPR signals are observed with $g_{\|}$ of 2.30 and 2.24, respectively, (b) the native intermediate at 2.02 mW and 77 K, in which only the T1 EPR signal is observed, and (c) the native intermediate taken at 0.5–25 W at 10 K, in which a new broad feature around 4000 G is observed. Simulations show that the native intermediate EPR signal in 'c' has g of 2.15, 1.86, and 1.65 (reproduced with permission from ref. [4], © 2002 American Chemical Society). (Right) Energy diagram of the ground and low-lying doublet states of the native intermediate, with depiction of the origin of the low g-value observed in 'c': when the two doublets are not spin–orbit coupled, the Zeeman energy levels (dotted lines) would be linearly dependent on the applied magnetic field (B), with $g > 2.0$ that corresponds to that of the individual Cu centers of the trinuclear Cu cluster. However, due to the spin–orbit coupling via antisymmetric exchange, the two doublet states are field-induced mixed and the Zeeman splitting is no longer linearly dependent on B. Consequently, the Zeeman splitting in each doublet is narrowed and the resonance field in the X-band radiation is shifted up in field, yielding low effective g-value of 1.65.

to the T2 Cu site is now absent (Fig. 8(b)). Importantly, at low temperature and high radiant power, a broad signal at ~4000 G is observed (Fig. 8(c)). This signal shows rapid relaxation and is not observed above 20 K. Simulations show that this broad signal has g-values of 2.15, 1.86, and 1.65. This new signal is difficult to saturate and exhibits very different saturation behavior compared to the T1 signal; the $P_{1/2}$, the microwave power at half-saturation, of the broad signal at 8.8 K is >25 mW, whereas that of the T1 signal is ~0.45 mW and that of the T2 signal (in the resting oxidized form) is ~0.05 mW. From the temperature dependence of the power saturation of the EPR and its Orbach analysis, and also from variable-temperature MCD, the presence of a low-lying excited doublet state has been estimated at ~150 cm^{-1} above the ground state [4].

Earlier studies have suggested that this new signal at ~4000 G, which also broadens with the use of $^{17}O_2$ isotope, is associated with a three-electron reduced oxyl or hydroxyl species with the T2 Cu center still reduced [40,41]. However, all four Cu centers in the NI have been determined to be oxidized by XAS edge studies [4]. In addition, a pair of intense and relatively broad field- and temperature-dependent MCD intensity with opposite signs (i.e. pseudo-A term; see Section 3) is observed in the CT region of the MCD spectrum of the NI that is very different from what is observed in the MCD spectrum of a hydroxyl radical [42]. Thus, XAS and MCD studies have provided definitive evidence that the NI form is not a radical species produced by a three-electron reduction of O_2, but rather a $4e^-$ reduced product of O_2 reduction with all four Cu centers oxidized.

With the insights gained from the model studies on TrisOH and μ_3O, it is possible to explain the unique ground state features of the NI based on the SOC phenomenon via antisymmetric exchange. On the right side of Fig. 8, the energy diagram of the ground and low-lying doublet states of the NI is presented with depiction of the origin of the new broad signal with low g-value. The dotted lines represent Zeeman energy levels when there are negligible SOC between the two doublets, while solid lines represent those when SOC is present. When the two doublets do not spin–orbit couple, the Zeeman energy levels would be linearly dependent on the applied magnetic field, with $g > 2.0$ that corresponds to those of the individual Cu(II) centers of the trinuclear Cu cluster. Alternatively, when there exists SOC via antisymmetric exchange, the two doublet states are mixed by the magnetic field and the Zeeman splitting is no longer linearly dependent on the field. Consequently, the Zeeman splitting in each doublet is narrowed and the resonance field in the X-band radiation is shifted up in field, yielding a low effective g-value of 1.65.

The extent of SOC between the ground and low-lying excited doublet states of the NI can be estimated by extending the theoretical model used for the ^2E ground state of TrisOH that includes symmetry lowering δ (an equilateral to isosceles ($J_{12} \neq J_{23} = J_{31}$ and $\delta = J_{12} - J_{23}$) distortion) and antisymmetric exchange factor G ($\approx G_z$). The experimental g-value of 2.15 is assumed to be the g_{eff} when the molecular z-axis normal to the Cu_3 plane is aligned with the applied magnetic field, while the g-values of 1.86 and 1.65 are assumed to be g_{eff} when the molecu-

lar z-axis is oriented perpendicular to the applied field. With $\Delta = \sqrt{\delta^2 + 3G^2} = 150\,\mathrm{cm}^{-1}$ (Eq. (6)), $\delta = 132 \pm 8\,\mathrm{cm}^{-1}$ and $G = 41 \pm 8\,\mathrm{cm}^{-1}$ are obtained. Given these values, the coefficient of mixing of the low-lying excited doublet state into the ground doublet state (or of the ground doublet state into the low-lying excited doublet state) is estimated to be ~6.2 (±2.5)%.

It is not possible to determine the geometric structure of the NI from the ground state analysis of TrisOH and μ_3O alone, as both structures allow large antisymmetric exchange via efficient ground-to-excited state superexchange interactions. Nonetheless, elucidation of the orbital origin of the low effective g-value of the NI delineates an interesting generalization for other antiferromagnetically coupled Cu(II) trimers: the EPR signal with a low g-value much less than 2.0 requires the presence of a low-lying excited doublet state that can effectively spin–orbit mix with the ground doublet state via antisymmetric exchange. Indeed, the EPR spectra of the azide treated resting oxidized [2] and the NI [43] forms of the tree laccase, both of which have mutually bridged trinuclear Cu cluster sites, show such EPR signals with low g-values.

3. Excited states of exchange coupled trimeric Cu(II) clusters

The ground state properties of TrisOH and μ_3O complexes allowed us to probe into the magnetic interactions among the Cu(II) spin centers. However, these properties do not allow a concrete distinction between different superexchange pathways. The effect of the antisymmetric and anisotropic exchange terms can be comparable, irrespective of what bridging ligands are present.

The metal–ligand bonding interactions in different environments can be directly probed using excited state methods, namely absorption, CD, and MCD spectroscopies. The electronic transition energies, intensities, band widths, and polarizations provide a direct probe of the ligand-field and the metal–ligand bonds [44,45]. In particular, MCD becomes powerful when measuring the weak d–d transition intensities as the d–d excited states are generally more spin–orbit mixed than ligand-based CT states, and therefore, d–d transitions typically show larger low temperature MCD intensity relative to absorption intensity (cf. ξ[Cu(II)] = 830 cm^{-1} versus ξ[O, N] ~ 60–70 cm^{-1}). Moreover, MCD intensities are closely related to the SOC between excited states. As the SOC involves essentially a single-center, one electron operator, elucidation of the nature of the MCD intensities and excited state SOC reveals a great deal of structural information on a metal–ligand chromophore.

3.1. The MCD C-term

The MCD intensity for a transition from a ground state $|A\rangle$ to an excited state $|J\rangle$ is described by [46,47]:

$$\frac{\Delta A}{E} = \frac{A_{\mathrm{LCP}} - A_{\mathrm{RCP}}}{E} = \gamma\beta B\left[-A_1\frac{\partial f(E)}{\partial E} + B_0 f(E) + \frac{C_0}{kT}f(E)\right] \quad (8)$$

where ΔA is the difference in the absorbed left- and right-circularly polarized light (=$A_{\mathrm{LCP}} - A_{\mathrm{RCP}}$), E the energy of the radiation, γ a collection of constants, β the Bohr magneton, B the applied magnetic field, and $f(E)$ is the band shape of the transitions. The first and second field-dependent terms ($\propto B$) in Eq. (8) are referred to as the MCD A- and B-terms, while the third field- and temperature-dependent term ($\propto B/T$) is referred to as the MCD C-term. The A_1-, B_0-, and C_0-parameters are first-order components of the A-, B-, and C-terms, where subscripts 0 and 1 imply that these are components of the zeroth- and first-order moments of the MCD transition. These parameters are given by specific mathematical expressions associated with the magnitudes and signs of the A-, B-, and C-terms that are dependent on the electronic and geometric structure of the molecule [46]. (Realize that "A", "B", and "J" have multiple meanings in this review: see Appendix A for summary of these symbols.)

Of the three MCD terms, the field- and temperature-dependent C-term [$\propto (B/T)C_0$] dominates the MCD intensity for paramagnetic systems with electronically degenerate ground states ($S \geq 1/2$) being several orders of magnitude larger than the field-only dependent A- and B-terms. Eq. (8) is appropriate for the linear limit where the temperature is high relative to the Zeeman splitting of the ground state sublevels. Alternatively, at low temperature when this limit is no longer appropriate, MCD C-terms exhibit saturation behavior. This phenomenon is utilized in the VTVH MCD experiments that can provide detailed descriptions of the ground spin state, the magnitude of the ZFS (as shown above for the ZFS of the ^{2}E ground state of TrisOH; Fig. 3), and the polarizations of the electronic transitions [45,48]. In the following sections, we focus on elucidating the MCD C-terms that are observed in the MCD spectra of the two Cu(II) model complexes. In particular, the origins of the C-term intensities are evaluated by correlating the geometric and electronic structures of the two model complexes to the properties of the C_0-parameters. Note that terms "C-term" and "C_0" are used in the text interchangeably; "C-term" will be used to indicate the observed, field-, and temperature-dependent MCD features, while "C_0" will be used when mathematical/physical formalisms are described. For detailed descriptions of the MCD A- and B-terms and a general overview of the MCD theory, refer to refs. [45,47].

The C_0-parameter for a spin allowed transition from a ground state $|A\rangle$ to an excited state $|J\rangle$ is given by:

$$C_0(A \rightarrow J) = -\frac{1}{|d_A|}\sum \langle A|\mu_z|A\rangle(|\langle A|m_-|J\rangle|^2 - |\langle A|m_+|J\rangle|^2) \quad (9)$$

where $|d_A|$ is the electronic degeneracy of the ground state $|A\rangle$, μ_z the z-component of the magnetic moment operator $\vec{\mu} = \vec{L} + 2\vec{S}$, and m_+ and m_- are the left- and right-circularly polarized electric dipole moments, respectively. In the laboratory-fixed coordinate system, the light travels along the z-direction, and the electric field components of the circularly polarized light are in the x,y-directions. In this coordinate frame, the electric dipole operator vectors have odd parity and m_+ and m_- are defined as $m_\pm = \mp(1/\sqrt{2})(m_x \pm \mathrm{i}m_y)$.

Eq. (9) takes both the light propagation and magnetic field directions to be along the molecular z-axis, which would be true for an oriented axial single crystal. However, most solution samples are studied as randomly oriented glasses or mulls, so that the random orientation of the magnetic field and light directions with respect to the ensemble of molecules in the sample must be taken into account. Thus, Eq. (9) can be rewritten as:

$$C_0(A \rightarrow J) = -\frac{i}{3|d_A|}\sum \langle A|\vec{\mu}|A\rangle \cdot (\langle A|\vec{m}|J\rangle \times \langle J|\vec{m}|A\rangle) \tag{10}$$

which can be further expanded as:

$$\begin{aligned} C_0(A \rightarrow J) = -\frac{i}{3|d_A|}\mathrm{Im}\sum [&\langle A|\mu_x|A\rangle(\langle A|m_y|J\rangle\langle J|m_z|A\rangle \\ &- \langle A|m_z|J\rangle\langle J|m_y|A\rangle) + \langle A|\mu_y|A\rangle(\langle A|m_x|J\rangle \\ &\times \langle J|m_z|A\rangle - \langle A|m_z|J\rangle\langle J|m_x|A\rangle) \\ &+ \langle A|\mu_z|A\rangle(\langle A|m_x|J\rangle\langle J|m_y|A\rangle \\ &- \langle A|m_y|J\rangle\langle J|m_x|A\rangle)] \end{aligned} \tag{11}$$

Eq. (11) shows that z-polarized transitions can also contribute to the MCD intensity, as long as there are three mutually orthogonal vectors, namely the direction of the applied magnetic field that gives rise to the ground state Zeeman terms and the two electric dipole moments between the ground and excited states.

It is important to note that, according to Eq. (11), either the ground state $|A\rangle$ or the excited state $|J\rangle$ must be spatially degenerate to have non-zero orbital angular momentum for two orthogonal transitions to be present, or either $|A\rangle$ or $|J\rangle$ must spin–orbit couple with a nearby state $|K\rangle$. The first case works when the molecule has high symmetry. However, it is more often the case that the molecule does not have high symmetry (i.e. a C_4 or C_3 symmetry axis) for its states to be spatially degenerate. In such cases, orbital angular momentum is quenched and this would eliminate the MCD intensity. Nevertheless, MCD C-term intensities (i.e. non-zero C_0) are observed experimentally and this necessitates departure from the zeroth-order description of the wave functions.

From perturbation theory, SOC allows non-zero C_0 and therefore, the C-term intensity to be present in the MCD spectrum of a molecule with low symmetry. When a transition $|A\rangle \rightarrow |J\rangle$ is polarized in only one direction, the other perpendicular transition that is required for the MCD intensity can be obtained from an intermediate excited state $|K\rangle$ that spin–orbit mixes into either $|A\rangle$ or $|J\rangle$ (note that such a SOC can occur with more than one intermediate state). The perturbed states $|A'\rangle$ and $|J'\rangle$, then, can be expressed as:

$$|A'\rangle = |A\rangle + \frac{i\hat{L}^{KA}}{\Delta_{KA}}|K\rangle \tag{12}$$

$$|J'\rangle = |J\rangle + \frac{i\hat{L}^{KJ}}{\Delta_{KJ}}|K\rangle \tag{13}$$

where $\Delta_{KA} = E_K - E_A$ and $\Delta_{KJ} = E_K - E_J$, and $\hat{L}^{KA}$ (equivalent definition for $\hat{L}^{KJ}$) which is the imaginary part of the purely imaginary SOC matrix element expressed as:

$$\hat{L}^{KA} = \mathrm{Im}\left\langle KS_{\mathrm{tot}}M_S^K \left| \sum_{N,i} \xi(r_{iN}) l_{N,w}(i) s_w(i) \right| AS_{\mathrm{tot}}M_S^A \right\rangle \tag{14}$$

$$\hat{L}^{KA} = -\hat{L}^{AK} \tag{15}$$

where $l_{N,w}(i)$ and $s_w(i)$ are w-components of the orbital and the spin angular momenta of the ith electron relative to nucleus N, and $M_S^K - M_S^A = 0$ or ± 1. The effective SOC parameter $\xi(r_{iN})$ is a function with $1/r^3$ dependence that makes SOC between different atomic centers negligible.

With substitution of the perturbed wave functions $|A'\rangle$ and $|J'\rangle$ into Eq. (11), the C_0-parameter for a spin-allowed transition between spatially non-degenerate doublet states $|A\rangle$ and $|J\rangle$ can be expressed as [48]:

$$\begin{aligned} C_0(A \rightarrow J) &= -\frac{1}{6}\sum_{uvw} g_w \sum_{K\neq A,J} [\Delta_{KJ}^{-1} L_w^{KJ}(D_u^{KA}D_v^{AJ} - D_v^{KA}D_u^{AJ}) \\ &\quad + \Delta_{KA}^{-1} L_w^{KA}(D_u^{AJ}D_v^{JK} - D_v^{AJ}D_u^{JK})] \end{aligned} \tag{16}$$

where g_w is the effective g-value of the doublet in the w-direction, L_w^{KA} and L_w^{KJ} the SOC matrix elements in the w-directions, and $D_u^{AJ} = \langle AS_{\mathrm{tot}}M_S|m_v|JS_{\mathrm{tot}}M_S\rangle$ $(=D_u^{JA})$ are the components of the transition dipole moment between $|A\rangle$ and $|J\rangle$ in the u-direction (equivalent definitions for D_u^{KA}, D_v^{AJ}, and D_v^{KA}). (Again, realize the symbol "D" has multiple meanings in this review: see Appendix A for summary of these symbols.)

The above formalism describes two mechanisms that allow the unidirectional $|A\rangle \rightarrow |J\rangle$ transition to gain MCD C-term intensity (i.e. non-zero C_0). In the first mechanism, in which $L_w^{KA} \approx 0$ and $L_w^{KJ} \neq 0$, a non-zero C_0 value is obtained by SOC between two nearby excited states $|J\rangle$ and $|K\rangle$ to which orthogonal transitions are made from a single ground state $|A\rangle$ (Scheme 9(a)). Also, when J and K in Eq. (16) are interchanged,

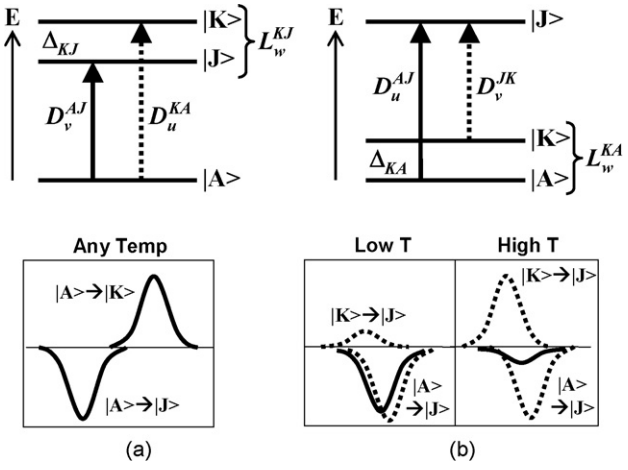

Scheme 9. (a and b) Reproduced with permission from ref. [12], ©2005 American Chemical Society.

the relationship

$$C_0(A \rightarrow K) = -C_0(A \rightarrow J) \quad (17)$$

is obtained, implying that the two orthogonal transitions $|A\rangle \rightarrow |J\rangle$ and $|A\rangle \rightarrow |K\rangle$ result in oppositely signed C-terms with equal intensities. Note that this pair of C-terms is called the "pseudo-A term" due to its derivative band shape similar to that of the MCD A-term. However, pseudo-A term is different from A-term, as the former is both field- and temperature-dependent (because it is, in fact, composed of two C-terms), whereas the latter is only field-dependent. Eq. (17) also illustrates the "MCD sum rule" that describes the requirement for spectral stability to conserve the total angular momentum of a photon [49]. In general, pseudo-A terms are observed in Cu(II) monomers which typically have a non-degenerate ground state that has small spin–orbit mixing with excited states due to large energy differences.

Alternatively, the second mechanism, in which $L_w^{KA} \neq 0$ and $L_w^{KJ} \approx 0$, describes the MCD intensity gained by SOC between the ground state $|A\rangle$ and a low-lying excited state $|K\rangle$ from which two orthogonal transitions can be made to a single excited state $|J\rangle$ (Scheme 9(b)). In the low temperature region where the low-lying excited state $|K\rangle$ is not populated, only the $|A\rangle \rightarrow |J\rangle$ transition is observed as a single MCD C-term while the $|K\rangle \rightarrow |J\rangle$ transition serves as a virtual orthogonal transition required for the MCD activity. Therefore, the MCD sum rule is not applicable. When the low-lying excited state $|K\rangle$ becomes populated at higher temperature, the $|K\rangle \rightarrow |J\rangle$ transition gains intensity with opposite C-term sign. If the energy splitting between $|A\rangle \rightarrow |J\rangle$ and $|K\rangle \rightarrow |J\rangle$ transitions is small, the $|K\rangle \rightarrow |J\rangle$ intensity cancels that of the $|A\rangle \rightarrow |J\rangle$ transition. Consequently, the observed C-term intensity would deviate from a linear dependence on $1/T$ at sufficiently high temperatures.

3.2. d–d transitions of TrisOH and μ_3O

The two contrasting MCD C-term intensity mechanisms described by the formalism of the C_0-parameter in Eq. (16) are observed in the d–d transition regions of the MCD spectra of TrisOH and μ_3O. The first mechanism, which accounts for SOC between two excited states (Scheme 9(a)), is found between 11,400 and 16,500 cm^{-1} energy region (bands 1–4) of the μ_3O MCD spectrum (Fig. 9) with weak absorption and strong MCD intensities [12]. In μ_3O, the d–d transitions are considered to be single site transitions and there is no low-lying orbital excited state that can spin–orbit couple into the ^{4}A ground state is limited. The relatively large C_0/D_0 ratios (≈MCD intensity/absorption intensity: see Appendix A for detailed description) are indicative of d–d transitions, involving large metal-based contributions to the orbitals in the transitions [50]. The band energies are also similar to the d–d energies of mononuclear Cu(II) complexes with similar geometries as the individual metal sites of μ_3O (i.e. distorted trigonal bipyramidal) [51]. MCD pseudo-A terms are observed, indicating that the intensities are governed by SOC between the associated excited states and that the spin–orbit mixing into the ground state is limited, as expected for a non-degenerate ^{4}A ground state. When the d–d excited states of μ_3O undergo SOC in the molecular z-direction (the molecular z-axis is ∼y-axis of each metal site; the z-axis of each metal site is along the Cu–O direction), two sets of pseudo-A terms are obtained [Fig. 9; $d_{xy}(+)/d_{yz}(-)$ and $d_{x^2-y^2}(+)/d_{xz}(-)$], similar to those observed in the MCD spectrum of a mononuclear Cu(II) complex [50].

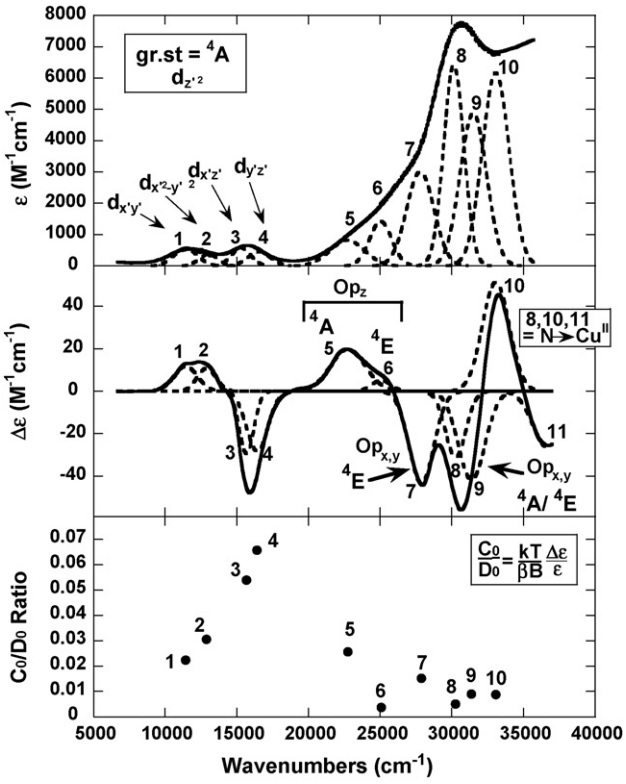

Fig. 9. μ_3O solution absorption (top, 10 K), MCD (middle, 5.0 K/7.0 T) spectra, and C_0/D_0 ratios (see Appendix A for definition) between the MCD and absorption intensities (bottom) (reproduced with permission from ref. [12], © 2005 American Chemical Society).

Alternatively, the second MCD intensity mechanism, which describes the MCD intensity gained by SOC between the ground state and a low-lying excited state (Scheme 9(b)), is observed in the 9400–15,900 cm^{-1} energy region (bands 1–4) of the TrisOH MCD spectrum (Fig. 10) [12]. As the data are taken from a mull sample, it is difficult to quantify the relative absorption and MCD intensities (i.e. C_0/D_0 ratio) to distinguish the d–d and CT transitions due to scattered light effects. However, the energies of bands 1–4 are similar to the d–d energies of mononuclear Cu(II) complexes with similar geometries as the individual metal sites in TrisOH (i.e. distorted square planar) [51]. These bands all have (−) C-terms, thus, deviating from the MCD sum rule. This indicates that their MCD intensity is governed by SOC between the ground state and a low-lying excited state (i.e. SOC between the zero-field split components of the ^{2}E) rather than SOC between excited states. Note that the intensity arising from the low-lying excited state at 65 cm^{-1} above the ground doublet state starts to contribute at $T > 30$ K. As described in Section 2, the intensity contribution from the low-lying excited state results in deviation of the $1/T$ Curie plot (Fig. 2) and VTVH

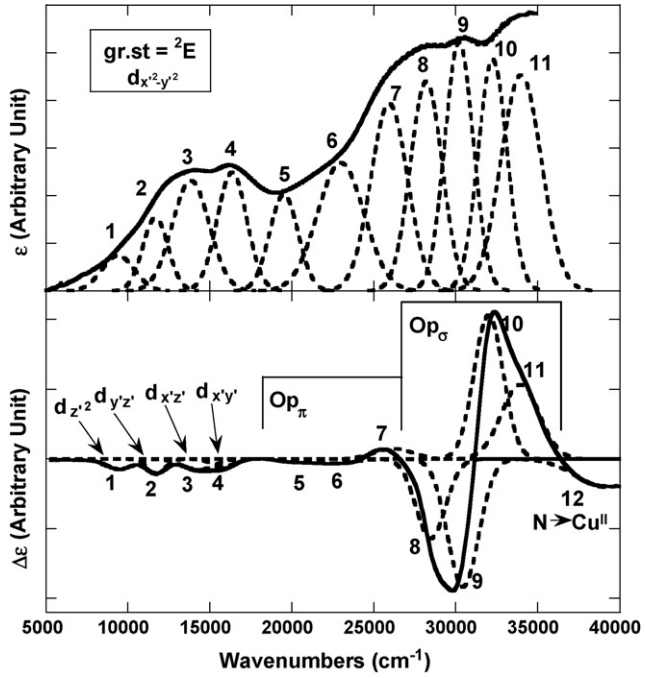

Fig. 10. TrisOH mull absorption (top, 10 K) and MCD (bottom, 5.0 K/7.0 T) spectra (reproduced with permission from ref. [12], ©2005 American Chemical Society).

MCD saturation plot (Fig. 3) from those of the typical $S_{tot} = 1/2$ system.

3.3. Charge transfer transitions

3.3.1. Excited state spin–orbit coupling leading to MCD pseudo-A terms

The SOC matrix element $\hat{L}^{KA}$ (and $\hat{L}^{AJ}$) in Eq. (14) is essentially a one-center function due to the $1/r^3$ dependence of the effective SOC parameter $\xi(r_{iN})$. Therefore, contributions that occur between different centers can be neglected, while a single atomic center must be simultaneously involved in both orthogonal CT transitions for MCD activity. Thus, elucidation of the underlying SOC mechanism leading to the MCD intensity would reveal a great deal of structural information for the SOC active chromophore under consideration.

The TrisOH and μ_3O structures possess two distinct orbital coupling mechanisms that allow SOC of two orthogonal O → Cu(II) CT transitions to produce the characteristic MCD pseudo-*A* terms present in their MCD spectra. Elucidation of the orbital origin of the pseudo-*A* term intensities of these model structures allows determination of the geometric and electronic structures of the exchange coupled trinuclear Cu(II) cluster in NI.

3.3.2. Metal-based spin–orbit coupling in TrisOH

Between 27,000 and 35,000 cm^{-1} of the TrisOH MCD spectrum (Fig. 10), intense and symmetric pseudo-*A* terms are observed with the (−) *C*-term components lower in energy by 2000–5000 cm^{-1}. These are determined to be all *x*,*y*-polarized by VTVH MCD, which shows no nesting behavior (at $T < 30$ K,

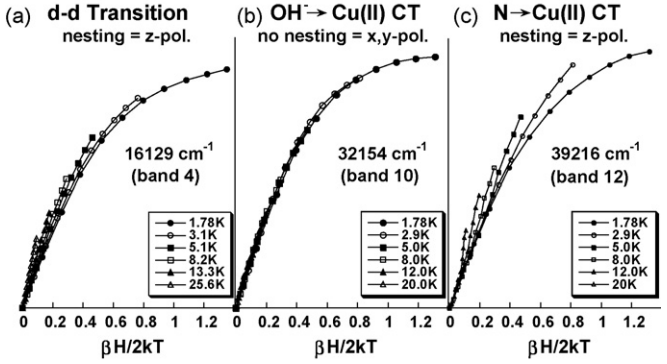

Fig. 11. Representative VTVH MCD plots of TrisOH mull sample at temperatures below 30 K. The d–d and the N → Cu(II) CT transitions in 'a' and 'c' show nesting behaviors indicating *z*-polarizations, while the OH$^-$ → Cu(II) CT transition in 'b' shows no nesting behavior indicating *x*,*y*-polarization (reproduced with permission from ref. [12], ©2005 American Chemical Society).

before the low-lying excited state is thermally populated (Fig. 11(b))). This is consistent with the positions of the OH$^-$ ligands being in the Cu_3 plane. On the other hand, the d–d and N → Cu(II) CT transitions exhibit nesting behavior at all temperatures (Fig. 11(a and c)), in spite of the $S_{tot} = 1/2$ ground state which typically shows no nesting behavior. The nesting derives from the non-linear dependence of the ground state energy levels on the magnetic field when the molecular *z*-axis is not aligned with the field (Scheme 2, $\theta > 0°$). Thus, the nesting indicates *z*-polarization: the *z*-polarization of the N → Cu(II) CT transitions is consistent with the N-ligands being out of the Cu_3 plane, while that of the d–d transitions is consistent with the fact that these transitions gain intensities from the *z*-polarized CT transitions at higher energies, such as the N → Cu(II) CT transitions.

The high intensities observed in both the absorption and MCD spectra imply strong Cu(II)–OH$^-$ σ-bonds. In addition, the *x*,*y*-polarized transition dipole moments require SOC matrix element in the *z*-direction, L_z, for MCD intensity. Thus, the C_0-parameter in Eq. (16), which describes the transition moment associated with the observed MCD *C*-term intensity, can be rewritten with consideration of SOC between two excited states $|J\rangle$ and $|K\rangle$:

$$C_0(A \rightarrow J) = -\frac{1}{6} \sum_{K \neq A,J} g_z \Delta_{KJ}^{-1} (D_x^{KA} D_y^{AJ} - D_y^{KA} D_x^{AJ}) L_z^{KJ} \quad (18)$$

Again, L_z is effectively a localized one-center function and the SOC center must be simultaneously involved in both orthogonal CT transitions. We first consider the OH$^-$-ligands as possible SOC centers since a CT state would involve the majority of the charge on the donor ligands. There are three different types of OH$^-$ p-orbitals: the first are the in-plane p-orbitals along the Cu–Cu directions that form strong Cu–O σ-bonds (=Op_σ), the second are the other in-plane p-orbitals involved in O–H bonds (=Op_H), and the third are the out-of-plane p-orbitals that form weak Cu–O π-bonds (=Op_π). The direction of the SOC is determined by rotating the donor Op_σ orbital at one oxygen center into either the Op_H or Op_π orbital of the same oxygen center. However, none of these orbital rotations yields L_z: rotation of

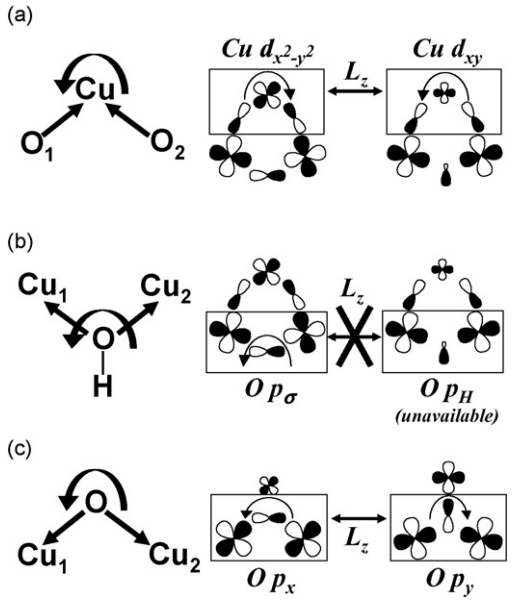

Fig. 12. Single-centered (a) metal-based spin–orbit coupling (SOC) in TrisOH, (b) OH-based SOC in TrisOH, and (c) oxo-based SOC in μ_3O. The OH-based SOC in TrisOH is disabled as the protonation eliminates one of the in-plane O p-orbitals (Op_H) for the spin–orbit rotation (reproduced with permission from ref. [12], © 2005 American Chemical Society).

an Op_σ into Op_π is possible only in the x- or y-direction that corresponds to L_x and L_y; although rotation into Op_H is possible in the z-direction, no significant spin–orbit mixing is expected since the energy differences between Op_σ and Op_H orbitals are large and the Op_H orbitals do not contribute in the Cu–O bonds or to the $OH^- \rightarrow$ Cu(II) CT transitions (Fig. 12(b)). Thus, a ligand OH^--based SOC cannot significantly contribute to the observed MCD pseudo-A terms.

Alternatively, transitions from two OH^- ligands to a single Cu site can be considered. In this case, the SOC would occur at the Cu centers, which is possible due to the highly covalent nature of the Cu–OH σ-bonds that allow a significant amount of metal contribution into the CT states. This metal-based SOC mechanism in the TrisOH structure is associated with the two donor MOs with $d_{x^2-y^2}$ and d_{xy} characters at the apex Cu center shown in Fig. 12(a), both of which are involved in σ-bonds with the in-plane Op_σ orbitals. The $d_{x^2-y^2}$ and d_{xy} characters can rotate into each other in the z-direction which generates L_z. Thus, the intense pseudo-A terms observed in the MCD spectrum of TrisOH derives from the SOC at the same Cu center between two different CT states that are involved in orthogonal CT transitions from two OH^--ligands to one Cu center. It is interesting to note that this metal-based SOC can also be very useful in explaining the MCD intensities of the ligand-to-metal CT transitions in many mononuclear transition metal complexes. In these complexes, a ligand-based SOC at the single donor ligand may not contribute significantly in the MCD intensity as the two required perpendicular transition moments cannot come from a single metal–ligand bond, the direction of a ligand-to-metal CT transition being along the metal–ligand vector. Instead, it is necessary to have a CT transition from another ligand to couple with the original CT transition via a metal-centered SOC.

There are eight CT excited states, $2^2A_1 + 2^2A_2 + 4^2E$, that are associated with the σ $OH^- \rightarrow$ Cu(II) CT transitions from the ^{2}E ground state in TrisOH. These transitions are all x,y-polarized. Therefore, in order for these transitions to gain MCD C-term intensities (i.e. non-zero C_0), each associated CT state must spin–orbit couple in the z-direction (i.e. L_z^{KJ} in Eq. (18)) with another CT state that is associated with a transition perpendicular to its own. Group theory predicts that the CT states are allowed to couple via L_z that induces either the out-of-state SOC ($^2A_1$–$^2A_2$ and ^{2}E–^{2}E) or the in-state SOC (^{2}E). However, the in-state SOC in the ^{2}E excited states of TrisOH are not expected to be resolved as the splittings would be determined either by the small SOC parameter of the ligand (ξ[O, N] ∼ 60–70 cm^{-1}) or by the significantly reduced contributions from the metal ions. The out-of-state CT state splittings, on the other hand, are directly related to the MO energy splittings of ∼4000 cm^{-1} obtained from DFT calculations [12], as the CT states would split in energy by the different bonding and exchange interactions. Therefore, the observed pseudo-A terms in the TrisOH MCD spectrum represent pairs of CT states that interact via out-of-state SOC.

Finally, the C-term signs (=signs of the C_0-parameters) can be evaluated by approximating the states $|A\rangle$, $|J\rangle$, and $|K\rangle$ with single determinantal wave functions, such as the broken symmetry DFT wave functions [48]. The procedure is illustrated in Fig. 13: (1) the acceptor and donor MOs are used to determine the signs of the transition dipole moments (D_x, D_y) and the SOC matrix element L_z, and then (2) the signs of D_x, D_y, and L_z are applied to Eq. (18) to predict the sign of the C_0-parameter, and thus, the C-term sign (=the sign of C_0) of the $|A\rangle \rightarrow |J\rangle$ transition. The C-term sign of the $|A\rangle \rightarrow |K\rangle$ transition would be opposite to that of the $|A\rangle \rightarrow |J\rangle$ transition, according to Eq. (17).

The metal-based SOC element L_z^{KJ} is obtained by the counterclockwise rotation of the SOC active orbital at the apex Cu center of the two donor MOs shown in Fig. 13. The rotation is made from the second donor MO (i.e. that represents $|K\rangle$) to that of the first donor MO (i.e. that represents $|J\rangle$) as the transitions are made from doubly occupied donor MOs to a singly occupied acceptor MO. Note that if the transitions are made from singly occupied donor MOs to an unoccupied acceptor MO (e.g. d–d transitions in d^1 systems), the rotation is made from the first donor MO to the second donor MO. The different sequences of the orbital rotations in the two cases are, in fact, related to the ligand-field treatment of the many-electron atomic SOC constants λ that are positive when orbitals are less than half-filled, but negative when more than half-filled. The signs of the transition dipole moments are obtained from the transition densities, which are the products of the donor and acceptor MO densities: the directions are taken from the center of the negative overlap (white) to that of the positive overlap (black) in the transition density.

Overall, we obtain $+D_x^{AJ}$, $+D_y^{KA}$, and $-L_z^{KJ}$. Substitution of these parameters into Eq. (18) yields (−) $C_0(A \rightarrow J)$ and (+) $C_0(A \rightarrow K)$ if $|K\rangle$ is higher in energy then $|J\rangle$ ($\Delta_{KJ} = E_K - E_J > 0$) and (+) $C_0(A \rightarrow J)$ and (−) $C_0(A \rightarrow K)$ if $|J\rangle$ is higher in energy then $|K\rangle$ ($\Delta_{KJ} < 0$) (Fig. 13). Notably, the lower energy C-term component of the pseudo-A term has negative sign and the higher

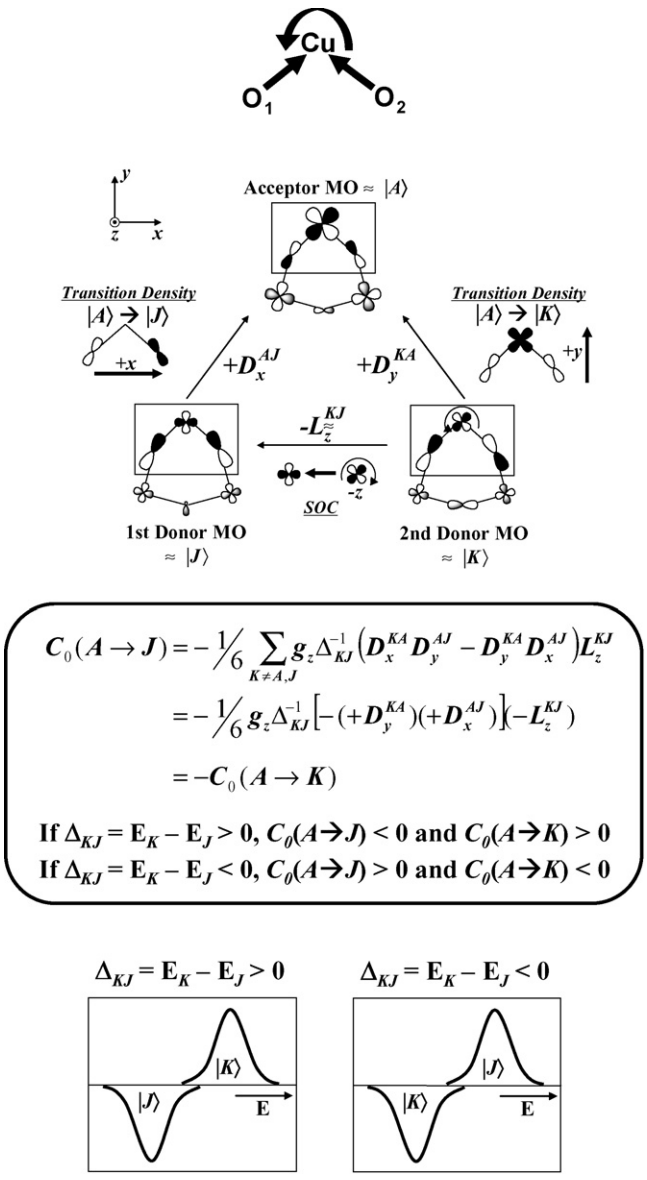

Fig. 13. Graphical prediction of the signs of the C_0-parameters (=signs of C-terms) of the σ OH^- → Cu(II) CT transitions in TrisOH. The acceptor MO, first donor MO, and second donor MO represent the ground state $|A\rangle$, the excited state $|J\rangle$, and the intermediate excited state $|K\rangle$. The counterclockwise rotation of the SOC active $d_{x^2-y^2}$ in the second donor MO to d_{xy} in the first donor MO yields negative overlap ($-L_z^{KJ}$). The directions taken from the center of the negative overlap (white) to that of the positive overlap (black) in the transition densities (the products of the donor and acceptor MO densities) define the signs of the transition moments ($+D_x^{AJ}$ and $+D_y^{KA}$). Application of these vector components into Eq. (18) yields a pseudo-A term with a negative low-energy C-term component, irrespective of the energy order of $|J\rangle$ and $|K\rangle$.

energy C-term component has positive sign, regardless of the relative energies of the two excited states $|J\rangle$ and $|K\rangle$. The predicted sign of the pseudo-A term is consistent with those observed in the MCD spectrum of TrisOH in Fig. 10.

3.3.3. Ligand-based spin–orbit coupling in μ_3O

The O^{2-} → Cu(II) CT transitions for μ_3O are associated with the asymmetrically shaped MCD pseudo-A terms with weak (+) C-terms (bands 5 and 6) and strong (−) C-terms (bands 7 and 9), the latter at 4000–9000 cm^{-1} higher in energy (Fig. 9). The corresponding absorption intensities are also asymmetric; e.g. band 9 is ∼7 times more intense than band 5. The relative absorption intensities reflect the donor orbital involved in these transitions. The strong intensities of bands 7 and 9 derive from the strong σ-bonds between the Cu d_{z^2} and the in-plane oxo p_x/p_y-orbitals, while the weak intensities of bands 5 and 6 derive from the weak pseudo-σ bonds between the Cu d_{z^2} and the out-of-plane oxo p_z-orbitals.

Group theory predicts six quartet CT excited states associated with O^{2-} → Cu(II) transitions, $3^4A + 3^4E$. From the ^4A ground state (recall that μ_3O has a ferromagnetic ground state, Section 2.3), the three $^4A \rightarrow {}^4A$ transitions would be z-polarized, while the three $^4A \rightarrow {}^4E$ transitions would be x,y-polarized. VTVH MCD show that bands 6, 7, and 9 are purely x,y-polarized, indicating these are the three available $^4A \rightarrow {}^4E$ transitions. Band 5, on the other hand, also has been determined to be dominantly x,y-polarized, but with ∼3% z-polarization. This band is, in fact, associated with the z-polarized $^4A \rightarrow {}^4A$ transition that derives from excitation of an electron between the bonding and anti-bonding MO pair that is associated with the weak pseudo-σ-bonds of the oxo p_z-orbitals and the three Cu d_{z^2}-orbitals. However, this transition is a purely z-polarized transition and MCD inactive, in contrast to what is determined from VTVH MCD.

The presence of the band 5 MCD intensity indicates that there is SOC between the ^4A state and an MCD active ^4E state. This intensity borrowing mechanism is described by:

$$\langle {}^4A_{gr} M_S | m_\pm | {}^4A M'_S \rangle = \frac{\langle {}^4E M_S | H_{SOC} | {}^4A M'_S \rangle \langle {}^4A_{gr} M_S | m_\pm | {}^4E M_S \rangle}{E({}^4E - {}^4A)} \quad (19)$$

where $^4A_{gr}$ is the ground state, H_{SOC} the SOC operator, $m_\pm$ is the electric dipole operator and $E(^4E - {}^4A)$ is the energy separation between the ^4E and ^4A excited states. Before the ^4A to ^4E out-of-state SOC, the $^4A_{gr} \rightarrow {}^4E$ transition will absorb both the left- and right-circularly polarized light that results in two oppositely signed C-terms that may or may not be resolved as a pseudo-A term, depending on the in-state spin–orbit splitting of the ^4E state. If the in-state spin–orbit splitting is too small, the C-terms will not be resolved as the intensities would cancel. Alternatively, if the out-of-state SOC becomes active, the ^4A and ^4E states are coupled via $L_xS_x + L_yS_y$ allowing the MCD-inactive $^4A \rightarrow {}^4A$ to gain intensity that involves only left-circularly polarized light.

In the μ_3O structure, SOC of any two orthogonal O^{2-} → Cu(II) CT transitions would occur at the central oxo-ligand. The in-plane oxo p_x- and p_y-orbitals are degenerate and can rotate into each other by L_z, while the out-of-plane oxo p_z-orbital can rotate into oxo p_x and p_y by L_y and L_x, respectively. As the SOC is oxo-based, the in-state splitting of the ^4E excited state is expected to be small and the intensities of the two oppositely signed C-terms of the $^4A \rightarrow {}^4E$ transition would cancel. However, if the positive C-term intensity is shifted into the ^4A state at band 5, the negative C-term component of the in-state pseudo-A term will no longer be canceled and a pseudo-A term of the two

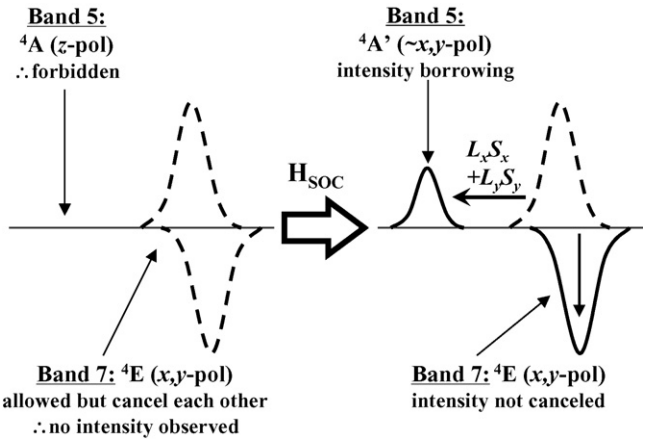

Scheme 10.

oppositely signed *C*-terms would result (Scheme 10). The SOC would involve rotation between the out-of-plane oxo p_z-orbital and the in-plane oxo p_x/p_y-orbitals in the *x*- or *y*-direction (i.e. $L_xS_x + L_yS_y$). As indicated by the relative absorption intensities, intense bands 7 and 9 are the ^{4}E states that derive from the oxo p_x/p_y donor orbitals. Therefore, the ^{4}A state associated with band 5, which derives from the oxo p_z-based donor orbital, can spin–orbit couple with these ^{4}E states to gain MCD intensity. More precisely, as the SOC matrix element L_w^{KJ} is one-electron operator, it is non-zero only when the determinants representing the two states differ by one electron occupation [48,52]. Therefore, it would be band 7 that effectively spin–orbit couples with band 5 as these two transitions share the same acceptor MO (the anti-bonding MO associated with the oxo p_z-orbital and the three Cu d_{z^2}-orbitals) and the resulting CT determinants differ by just one electron occupation. Band 9, which is associated with excitation of the oxo p_x/p_y-based donor MO to the oxo p_x/p_y-based acceptor MO, would not be effective in SOC with band 5 as the resulting CT determinant would differ by two electron occupations.

Finally, recall that a μ_3-oxo structure can also have an antiferromagnetic ^{2}E ground state if the oxo-ligand is close to the Cu_3 plane (Scheme 7, right). Therefore, we evaluate the electronic transition properties of an antiferromagnetically coupled μ_3O, especially for the purpose of extrapolating the experimental quartet μ_3O model complex to the doublet ground state of the NI. If the oxo-ligand is in the Cu_3 plane, contributions from the out-of-plane oxo p_z-orbital in the Cu–O bonds can be neglected. For the oxo $p_{x,y} \rightarrow$ Cu(II) CT transitions, eight CT excited states, $4^2A + 4^2E$, are available. Similar to the TrisOH case, all CT transitions from the ^{2}E ground state to these states are *x*,*y*-polarized (thus, MCD allowed) that can be coupled via L_z, either by the out-of-state SOC (^{2}A–^{2}A and ^{2}E–^{2}E) or the in-state SOC (^{2}E). With the oxo-based SOC (between the oxo p_x- and p_y-orbitals, Fig. 12(c)), the in-state splitting of a ^{2}E CT state would be small and not produce a significant MCD feature. Alternatively, the CT states would be separated by at least ~1500 cm^{-1}, as indicated by the broken symmetry DFT calculations [12]. Therefore, it is possible to have out-of-state SOC of the eight available CT states to form four pseudo-*A* terms.

The signs of the *C*-terms (=signs of the C_0-parameters) of a μ_3O structure having a ground doublet state can be predicted following the same procedure as for TrisOH (see above). Here, the oxo-based SOC element L_z^{KJ} is obtained by the counterclockwise rotation of the SOC active orbital at the oxo center of the two donor MOs shown in Fig. 14: rotation of the oxo p_x-orbital

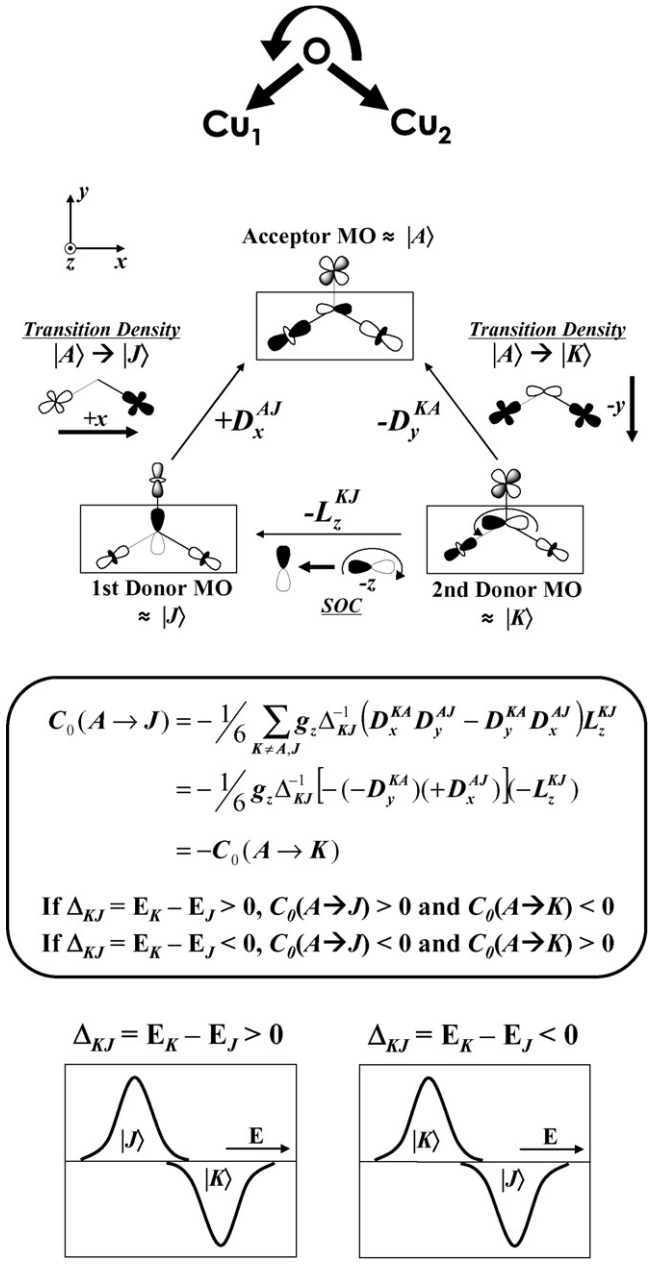

Fig. 14. Graphical prediction of the signs of the C_0-parameters (=signs of *C*-terms) of the σ $O^{2-} \rightarrow$ Cu(II) CT transitions of μ_3O. The acceptor MO, first donor MO, and second donor MO represent the ground state $|A\rangle$, the excited state $|J\rangle$, and the intermediate excited state $|K\rangle$. The counterclockwise rotation of the SOC active p_x in the second donor MO to p_y in the first donor MO yields negative overlap ($-L_z^{KJ}$). The directions taken from the center of the negative overlap (white) to that of the positive overlap (black) in the transition densities (the products of the donor and acceptor MO densities) define the signs of the transition moments ($+D_x^{AJ}$ and $-D_y^{KA}$). Application of these vector components into Eq. (18) yields a pseudo-*A* term with a positive low-energy *C*-term component, irrespective of the energy order of $|J\rangle$ and $|K\rangle$.

in the second donor MO ($\approx|K\rangle$) to the oxo p_y-orbital of the first donor MO ($\approx|J\rangle$). Overall, we obtain $+D_x^{AJ}$, $-D_y^{KA}$, and $-L_z^{KJ}$. Substitution of these parameters into Eq. (18) yields (+) $C_0(A \rightarrow J)$ and (−) $C_0(A \rightarrow K)$ if $|K\rangle$ is higher in energy then $|J\rangle$ ($\Delta_{KJ} > 0$), and (−) $C_0(A \rightarrow J)$ and (+) $C_0(A \rightarrow K)$ if $|J\rangle$ is higher in energy then $|K\rangle$ ($\Delta_{KJ} < 0$). Thus, the sign of the pseudo-*A* term is the same regardless of the relative energies of the two excited states $|J\rangle$ and $|K\rangle$ (Fig. 14), as with TrisOH. However, the sign of the pseudo-*A* term with positive lower energy and negative higher energy *C*-term components is opposite to that of TrisOH. Notably, the predicted signs of the pseudo-*A* terms are unique for each Cu_3 structure as specific MO descriptions have been utilized in these predictions.

3.4. Excited states of the native intermediate

The low temperature (5 K) MCD and room temperature absorption spectra of the *R. vernicifera* tree laccase NI, with simultaneous Gaussian fits, are presented in Fig. 15. The O → Cu(II) CT transitions are bands 9–12 with strong absorption and MCD intensities; the intense band 5 is associated with the Cys S → T1 Cu(II) CT transition that gives the bluish color for both the resting oxidized and NI forms of the tree laccase. The characteristic MCD pseudo-*A* terms formed by bands 9–12

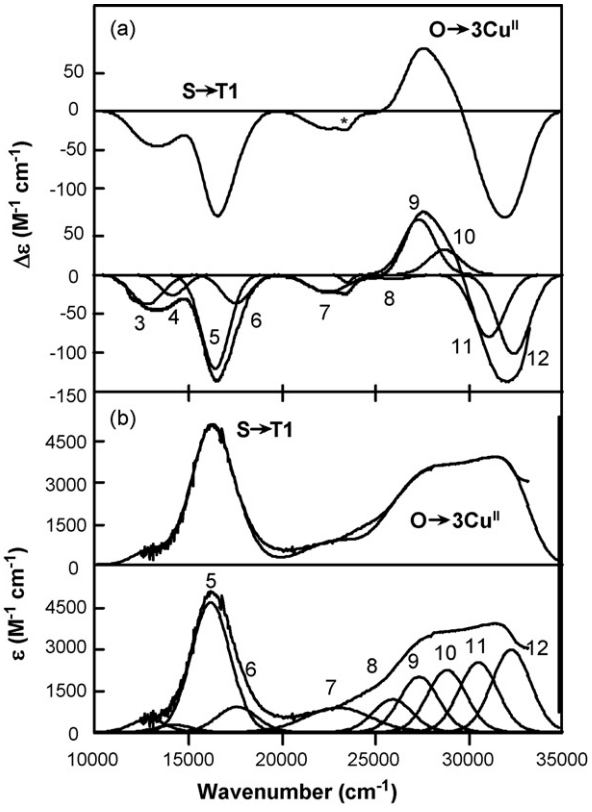

Fig. 15. (a) Room temperature absorption and (b) low temperature MCD spectra of the native intermediate with simultaneous Gaussian fits. The highly intense bands 9–12 that form pseudo-*A* terms in the MCD spectrum are the O → Cu(II) CT transitions (the intense band 5 is associated with the S → T1 Cu(II) CT transitions) (reproduced with permission from ref. [4], ©2002 American Chemical Society).

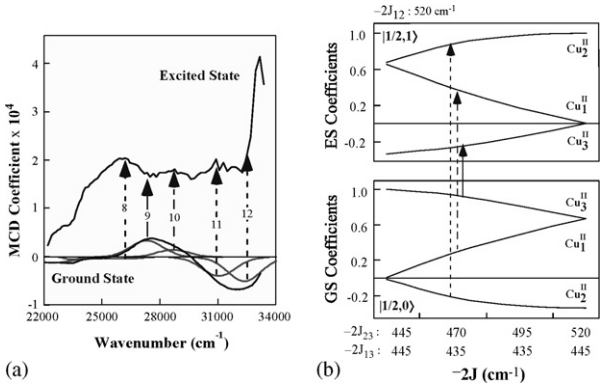

Fig. 16. (a) The ground and excited state MCD spectra of the native intermediate. Gaussian fit of the ground state spectrum is shown in gray. Different arrows indicate the different Cu centers associated with the CT transitions. (b) Coupling coefficients of the individual Cu's of the trinuclear Cu(II) cluster in the ground state (GS) and excited state (ES) wave functions. Different arrows indicate the different Cu's associated with the CT transitions, according to the three inequivalent exchange coupling constants in the trinuclear Cu cluster of the native intermediate (reproduced with permission from ref. [4], © 2002 American Chemical Society).

have positive low energy and negative high energy *C*-term components, similar to that predicted for the antiferromagnetically coupled μ_3O (Fig. 14). Moreover, the ground and excited state MCD spectra, obtained from variable-temperature MCD experiments, have allowed determination of the different contributions of the individual Cu centers in the ground and excited state wave functions (Fig. 16) [4]. As indicated by different arrows connecting the ground and excited state spectra in Fig. 16, band 9 changes from (+) to (−), band 10 remains (+) to (+), and bands 11 and 12 change from (−) to (+). These different behaviors originate from the inequivalent ligand-field structures of the Cu centers and different exchange coupling coefficients of the three Cu pairs in the trinuclear cluster ($-2J = 435$, 470, and 520 cm^{-1}) [4]. As a result, the spin densities localize on to individual Cu centers in the trinuclear cluster and contribute differently in the ground and the low-lying excited state trimer wave functions. Thus, the pseudo-*A* term of the NI corresponds to CT transitions to the different Cu centers of the trinuclear cluster.

Considering the two distinct SOC mechanisms in the MCD pseudo-*A* term intensities of TrisOH and μ_3O, it is now possible to eliminate TrisOH as a model for NI since its MCD intensity mechanism requires the two *C*-term components of a pseudo-*A* term to be associated with CT transitions to the same Cu center (Fig. 12(a)). μ_3O, on the other hand, requires an oxo-based SOC mechanism that couples CT transitions to two different Cu centers, consistent with NI (Fig. 12(c)). Moreover, the sign of the pseudo-*A* term of NI is opposite to that experimentally observed and theoretically predicted for TrisOH (Figs. 10 and 13), but is in accordance with that predicted for the antiferromagnetically coupled μ_3O (Fig. 14), which adds further support for the μ_3-oxo bridged structure.

With the proposition that the trinuclear Cu cluster in NI has a μ_3-oxo bridging ligand, it is now possible to make a more detailed assignment to bands 9–12 in Fig. 15. The T2 site

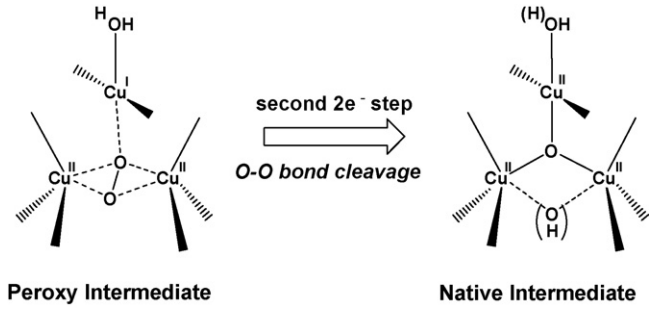

Scheme 11.

would have a four-coordinate square planar site with the μ_3-oxo ligand, two histidines, and a OH^-/H_2O ligand, while each of the T3 Cu centers would have the μ_3-oxo ligand and three histidines (Scheme 11, right). The μ_3-oxo ligand would now occupy what was coordinatively unsaturated sites for the three Cu centers in the resting oxidized form (cf. Scheme 8) [38,39]. Note that an extra OH^- bridge can exist between the T3 Cu centers that would be the second oxygen product of the O–O bond cleavage. It is not clear from the current analysis whether this ligand remains at the trinuclear site or whether it is dissociated, as the $OH^- \rightarrow$ Cu(II) CT transitions would not show up distinctively in the MCD spectrum (see above, Fig. 12). Depending on the presence of the OH^- ligand, the T3 Cu centers would be either four-coordinated tetrahedral or five-coordinated trigonal bipyramidal/square pyramidal sites (Scheme 11, right).

The splitting of the *C*-terms in the pseudo-*A* features of the NI strongly depends on the relative energies of the singly occupied acceptor d-orbitals at the two Cu sites that are involved in the oxo $\rightarrow Cu^{II}$ CT transitions. In the context of ligand-field theory, the T2 Cu site has a square planar ligand field that destabilizes the acceptor orbitals (by ~4000–5000 cm^{-1}) relative to the ligand field environment of the T3 Cu sites. Furthermore, it is possible that the water derived ligand at T2 site is deprotonated and the strong donor character of the OH^- ligand at the T2 site would destabilize the acceptor d-orbital by an additional several thousand cm^{-1}. Overall, it is likely that the acceptor d-orbital of the T2 Cu is higher in energy than those of the T3 Cu's. Therefore, the two higher energy (−) *C*-terms (bands 11 and 12, Fig. 15) would correspond to the μ_3-oxo $\rightarrow$ T2 Cu(II) CT transitions and the two lower energy (+) *C*-terms (bands 9 and 10) would correspond to the μ_3-oxo $\rightarrow$ T3 Cu(II) CT transitions.

Assignment of the internal μ_3-oxo bridged structure for the NI now allows us to further deduce a plausible structure for the precursor peroxy intermediate (PI) and formulate the reaction coordinate of O–O bond cleavage in the second $2e^-$ step of the $4e^-$ reduction of O_2 (Scheme 11). The PI would have an internally bridged peroxide that is bonded to the two oxidized T3 Cu centers, as well as to the reduced T2 Cu center (Scheme 11, left); a QM/MM study also reports such a binding mode in the PI [53]. Importantly, the T2 Cu(I)–peroxide bonding interaction would allow facile electron transfer from the T2 Cu(I) to the peroxide, leading to a rapid reductive cleavage of the O–O bond (note that the second electron required in this second $2e^-$ step comes from the T1 site). The resulting Cu(II)–O σ-bonding interactions and exchange coupling in the NI would provide a thermodynamic driving force as these would induce a significant decrease in the reduction potentials of the Cu centers.

The μ_3-oxo bridge in NI also implicates efficient electron transfer that allows fast reduction of the fully oxidized NI back to the fully reduced form. Note that the reduction rate of the resting enzyme is too slow to be catalytically relevant, as the T2 site is electronically isolated from the T3 centers. Alternatively, the NI has effective superexchange pathways that facilitate rapid electron transfer from the T1 site to all the Cu centers in the trinuclear cluster via the strong Cu–O σ-bonds. Thus, the exchange coupled NI structure is the catalytically relevant fully oxidized form of the multicopper oxidases, with the μ_3-oxo bridge allowing efficient reduction and turnover with O_2 in the enzymatic cycle.

Finally, the internally bound μ_3-oxo structure in NI is consistent with the slow decay of the NI to the resting enzyme. Previous studies, using ^{18}O isotope ratio mass spectrometry [3,54] and ^{17}O EPR [41], have suggested that only one oxygen atom of O_2 is present after turnover in the resting enzyme that is bound terminally to the T2 Cu center. This would be the OH^- ligand on the T2 site that lies outside the trinuclear cluster. As this oxygen atom likely derives from the μ_3-oxo ligand of the NI, the decay process would require a large structural reorganization of this atom from inside to outside of the cluster, resulting in a slow decay process.

4. Conclusions

In this review, we have provided detailed spectroscopic descriptions of the ground and excited state properties of two representative exchange coupled trinuclear Cu(II) cluster complexes. Single crystal/powder EPR and VTVH MCD have provided direct experimental probes for the ground state wave functions in the antiferromagnetically coupled TrisOH and ferromagnetically coupled μ_3O complexes and lead to the demonstration of the ZFS in the ground states via SOC, provided by the antisymmetric and anisotropic exchange interactions. The orbital descriptions of the ground-to-ground and the ground-to-excited state superexchange interactions in these complexes further led to important molecular level understanding of the nature of the spin frustrated ground state of the NI and the origin of the low *g*-value of its EPR signal.

We have also elucidated the physical origin of the intense pseudo-*A* term in the MCD spectrum of the NI. A detailed electronic structural analysis of the two model complexes led to two distinct SOC mechanisms required for the observed pseudo-*A* terms associated with the $OH^-/O^{2-} \rightarrow$ Cu(II) CT transitions: two transitions to the same Cu center with a metal-centered SOC are required for TrisOH, while transitions to two different Cu centers with an oxo-based SOC are required for μ_3O. Accordingly, we were able to conclude that the spectroscopic features from the trinuclear Cu cluster in NI are consistent only with the μ_3-oxo bridged structure. Thus, MCD has proven to be

extremely powerful in revealing a great deal of structural information for the determination of this key enzymatic intermediate and in providing a general mechanism for the assignment of CT transitions.

The fundamental descriptions of the geometric, electronic structures and the bonding interactions in the exchange coupled trinuclear Cu(II) clusters have provided important mechanistic implications in the reactivity of the multicopper oxidases. Extensive spectroscopic and DFT studies are underway to elucidate the energy profile related to the O_2 activation in the first and second $2e^-$ steps of the O_2 reduction in multicopper oxidases, as well as in the fast re-reduction of the NI in the turnover step of the catalytic cycle and the slow decay of the NI to the resting enzyme.

Acknowledgments

This research was supported by NIH Grant DK31450 (E.I.S.). J.Y. gratefully acknowledges a Franklin Veatch Memorial Fellowship.

Appendix A. Summary of symbols used with multiple meanings

Based on common usage, we have necessarily used symbols (A, B, D, G, J, and Δ) with multiple meanings in this review, as both the fields of EPR and MCD spectroscopies are covered. To avoid confusion, refer to the following table that includes the location and description of each symbol:

Symbols	Location	Description
A, $A_\parallel$, $A_\perp$	Section 2	Metal hyperfine splitting values
ΔA	Section 3.1, Eq. (8)	Difference in the absorption of the left- and right-circularly polarized light ($=A_{LCP} - A_{RCP}$)
A-Term	Section 3.1	Field-dependent MCD intensity with a derivative band shape
$\|A\rangle$	Section 3	Ground state wave function
A_1	Section 3.1, Eq. (8)	First-order component of the field-dependent MCD A-term that has a derivative band shape. Subscript "1" indicates this is a component of the first-order moment of the electronic transition
Pseudo-A term	Section 3	A set of field- and temperature-dependent MCD C-terms that have nearly equal intensities and opposite signs. The nomenclature comes from its derivative shape similar to that of the MCD A-term. However, it is not equivalent to the A-term since the two bands in a pseudo-A term are both field- and temperature-dependent as these are, in fact, MCD C-terms. The opposite signs originate from the interaction of the two transitions via spin–orbit coupling
B	Whole manuscript	Applied magnetic field
B_0	Section 3.1, Eq. (8)	First-order component of the field-dependent MCD B-term that has an absorption band shape. Subscript "0" indicates this is a component of the zeroth-order moment of the electronic transition
B-Term	Section 3.1	Field-dependent MCD intensity with an absorption band shape
C-Term	Section 3	Field- and temperature-dependent MCD intensity that has an absorption band shape
C_0	Section 3, Eqs. (8)–(11), (16)–(18)	First-order component of the field- and temperature-dependent MCD C-term. Subscript "0" indicates this is a component of the zeroth-order moment of the electronic transition. Its magnitude is estimated from the field- and temperature-dependent MCD C-term intensity
C_0/D_0 ratio	Section 3.2	Ratio of the MCD C_0-parameter and dipole strength D_0 of an electronic transition. Experimentally, this ratio is estimated using: $C_0/D_0 = (kT/\beta B)(\Delta\varepsilon/\varepsilon) \approx 1.064(\Delta\varepsilon/\varepsilon)$ [at $B = 7$ T and $T = 5$ K], where ε is the molar extinction coefficient obtained from absorption (i.e. Beer's Law) and $\Delta\varepsilon$ is the difference between the molar extinction coefficients for left- and right-circularly polarized light. The latter is obtained from the MCD intensity and converted using: $\Delta\varepsilon = \psi/(32.98 \times l \times c)$, where ψ is the ellipticity (mdeg) (≈the observed MCD intensity), l the light path length (cm), and c is the concentration (mM)
D	Section 2, Eqs. (2) and (4)	Spin Hamiltonian parameter for the anisotropic exchange
d_A	Section 3, Eqs. (9)–(11)	Electronic degeneracy of the ground state $\|A\rangle$
D_0	Section 3.2	Dipole strength (zeroth-order moment) of an electronic transition associated with the absorption intensity (also see C_0/D_0 ratio)
D_u^{KA}	Section 3, Eqs. (16) and (18)	u-Component of the transition dipole moment of the $\|A\rangle \rightarrow \|K\rangle$ electronic transition
g, $g_\parallel$, $g_\perp$, g_w	Whole manuscript	g-Factor
G, G_z	Section 2	Spin Hamiltonian parameter for the antisymmetric exchange
J	Whole manuscript	Spin Hamiltonian parameter for the isotropic exchange constant
$\|J\rangle$	Section 3	Excited state wave function used in Section 3
δ, δ'	Section 2, Eqs. (5)–(7)	Difference in the isotropic exchange coupling constants of a trimer, implying a symmetry lowering effect
Δ	Section 2, Eqs. (6) and (7)	Zero-field splitting of the ^{2}E ground state of a Cu(II) trimer

Appendix A. (*Continued*)

Symbols	Location	Description
Δ_1, Δ_2	Section 2.1, Eqs. (3) and (4)	Energy difference between the ground and excited states of the individual metal centers 1 and 2 of an exchange coupled metal pair
Δ_{KA}	Section 3.1, Eqs. (12) and (13)	Energy difference between molecular states $\|K\rangle$ and $\|A\rangle$

References

[1] (a) E.I. Solomon, P. Chen, M. Metz, S.-K. Lee, A.E. Palmer, Angew. Chem. Int. Ed. 40 (2001) 4570;
(b) E.I. Solomon, U.M. Sundaram, T.E. Machonkin, Chem. Rev. 96 (1996) 2563.

[2] (a) M.D. Allendorf, D.J. Spira, E.I. Solomon, Proc. Natl. Acad. Sci. U.S.A. 82 (1985) 3063;
(b) D.J. Spira-Solomon, M.D. Allendorf, E.I. Solomon, J. Am. Chem. Soc. 108 (1986) 5318.

[3] W. Shin, U.M. Sundaram, J.L. Cole, H.H. Zhang, B. Hedman, K.O. Hodgson, E.I. Solomon, J. Am. Chem. Soc. 118 (1996) 3202.

[4] S.-K. Lee, S. DeBeer George, W.E. Antholine, B. Hedman, K.O. Hodgson, E.I. Solomon, J. Am. Chem. Soc. 124 (2002) 6180.

[5] J.L. Cole, D.P. Ballou, E.I. Solomon, J. Am. Chem. Soc. 113 (1991) 8544.

[6] A.E. Palmer, S.-K. Lee, E.I. Solomon, J. Am. Chem. Soc. 123 (2001) 6591.

[7] J. Yoon, L.M. Mirica, T.D.P. Stack, E.I. Solomon, J. Am. Chem. Soc. 126 (2004) 12586.

[8] L.M. Mirica, T.D.P. Stack, Inorg. Chem. 44 (2005) 2131.

[9] M.P. Suh, M.Y. Han, J.H. Lee, K.S. Min, C. Hyeon, J. Am. Chem. Soc. 120 (1998) 3819.

[10] M.C. Kozlowski, X. Li, P.J. Carroll, Z. Xu, Organometallics 21 (2002) 4513.

[11] (a) P.A. Angaridis, P. Baran, R. Boča, F. Cervantes-Lee, W. Haase, G. Mezei, R.G. Raptis, R. Werner, Inorg. Chem. 41 (2002) 2219;
(b) R.J. Butcher, C.J. O'Conner, E. Sinn, Inorg. Chem. 20 (1981) 537.

[12] J. Yoon, L.M. Mirica, T.D.P. Stack, E.I. Solomon, J. Am. Chem. Soc. 127 (2005) 13680.

[13] J. Yoon, E.I. Solomon, Inorg. Chem. 44 (2005) 8076.

[14] (a) E. Sinn, Coord. Chem. Rev. 5 (1970) 313;
(b) J.S. Griffith, Struct. Bond. 10 (1972) 87;
(c) G.F. Kokoszka, R.W. Duerst, Coord. Chem. Rev. 5 (1970) 209.

[15] R.D. Cannon, R.P. White, Prog. Inorg. Chem. 36 (1988) 195.

[16] B.S. Tsukerblat, M.I. Belinskii, V.E. Fainzil'berg, Sov. Sci. Rev. B Chem. 9 (1987) 337.

[17] (a) F.B. Hulsbergen, R.W.M. ten Hoedt, G.C. Verschoor, J. Reedijk, A.L. Spek, J. Chem. Soc. Dalton Trans. (1983) 539;
(b) J.-P. Costes, F. Dahan, J.-P. Laurent, Inorg. Chem. 25 (1986) 413;
(c) M. Angaroni, A. Ardizzoia, T. Beringhelli, G. La Monica, D. Gatteschi, N. Masciocchi, M. Moret, J. Chem. Soc. Dalton Trans. (1990) 3305.

[18] (a) S. Ferrer, J.G. Haasnoot, J. Reedijk, E. Müller, M. Biagini Cingi, M. Lanfranchi, A.M. Manotti Lanfredi, J. Ribas, Inorg. Chem. 39 (2000) 1859;
(b) S. Ferrer, F. Lloret, I. Bertomeu, G. Alzuet, J. Borrás, S. García-Granda, M. Liu-González, J.G. Haasnoot, Inorg. Chem. 41 (2002) 5821;
(c) H. López-Sandoval, R. Contreras, A. Escuer, R. Vicente, S. Bernès, H. Nöth, G.J. Leigh, N. Barba-Behrens, J. Chem. Soc. Dalton Trans. (2002) 2648;
(d) X. Liu, M.P. de Miranda, E.J.L. McInnes, C.A. Kilner, M.A. Halcrow, Dalton Trans. (2004) 59.

[19] H.T. Diep (Ed.), Frustrated Spin Systems, World-Scientific, Singapore, 2004.

[20] (a) A.P. Ramirez, Annu. Rev. Mater. Sci. 24 (1994) 453;
(b) J.E. Greedan, J. Mater. Chem. 11 (2001) 37.

[21] S. Nakatsuji, Y. Nambu, H. Tonomura, O. Sakai, S. Jonas, C. Broholm, H. Tsunetsugu, Y. Qui, Y. Maeno, Science 309 (2005) 1697.

[22] G. Toulouse, Commun. Phys. 2 (1977) 115.

[23] (a) J. Villain, J. Phys. C 10 (1977) 1717;
(b) J. Villain, Z. Phys. 33 (1979) 31.

[24] (a) T. Moriya, Phys. Rev. 120 (1960) 91;
(b) T. Moriya, in: G.T. Rado, H. Suhl (Eds.), Magnetism, vol. 1, Academic Press, New York, 1963, p. 85.

[25] I. Dzyaloshinsky, J. Phys. Chem. Solids 4 (1958) 241.

[26] A. Bencini, D. Gatteschi, Electron Paramagnetic Resonance of Exchange Coupled Systems, Springer-Verlag, Berlin, 1990.

[27] J. Kanamori, in: G.T. Rado, H. Suhl (Eds.), Magnetism, vol. 1, Academic Press, New York, 1963, p. 127.

[28] O. Kahn, Molecular Magnetism, VCH, New York, 1993.

[29] (a) N.D. Chasteen, R.L. Belford, Inorg. Chem. 9 (1970) 169, 2805;
(b) M. Chikira, H. Kon, R.A. Hawley, K.M. Smith, J. Chem. Soc. Dalton Trans. (1979) 245.

[30] Yu.V. Rakitin, Yu.V. Yablokov, V.V. Zelentsov, J. Magn. Reson. 43 (1981) 288.

[31] T. Murao, Phys. Lett. 49A (1974) 33.

[32] (a) B. Cage, F.A. Cotton, N.S. Dalal, E.A. Hillard, B. Rakvin, C.M. Ramsey, J. Am. Chem. Soc. 125 (2003) 5270;
(b) R. Clérac, F.A. Cotton, K.R. Dunbar, E.A. Hillard, M.A. Petrukhina, B.W. Smucker, C.R. Acad. Sci. Paris, Chim./Chem. 4 (2001) 315.

[33] P.K. Ross, M.D. Allendorf, E.I. Solomon, J. Am. Chem. Soc. 11 (1989) 4009.

[34] (a) L. Banci, A. Bencini, D. Gatteschi, J. Am. Chem. Soc. 105 (1983) 761;
(b) L. Banci, A. Bencini, D. Gatteschi, Inorg. Chem. 23 (1984) 2138;
(c) M.-F. Charlot, Y. Journaux, O. Kahn, A. Bencini, D. Gatteschi, C. Zanchini, Inorg. Chem. 25 (1986) 1060.

[35] P.J. Hay, J.C. Thibeault, R. Hoffmann, J. Am. Chem. Soc. 97 (1975) 4884.

[36] E.I. Solomon, R.K. Szilagyi, S. DeBeer George, L. Basumallick, Chem. Rev. 104 (2004) 419.

[37] (a) K.W. Penfield, R.R. Gay, R.S. Himmelwright, N.C. Eickman, V.A. Norris, H.C. Freeman, E.I. Solomon, J. Am. Chem. Soc. 103 (1981) 4382;
(b) S.E. Shadle, J.E. Penner-Hahn, H.J. Schugar, B. Hedman, K.O. Hodgson, E.I. Solomon, J. Am. Chem. Soc. 115 (1993) 767.

[38] L. Quintanar, J. Yoon, C.P. Aznar, A.E. Palmer, K.K. Andersson, R.D. Britt, E.I. Solomon, J. Am. Chem. Soc. 127 (2005) 13832.

[39] (a) A. Messerschmidt, R. Ladenstein, R. Huber, M. Bolognesi, L. Avigliano, R. Petruzzelli, A. Rossi, A. Finazzi-Agró, J. Mol. Biol. 224 (1992) 179;
(b) I. Zaitseva, V. Zaitsev, G. Card, K. Moshkov, B. Bax, A. Ralph, P. Lindley, J. Biol. Inorg. Chem. 1 (1996) 15;
(c) T. Bertrand, C. Jolivalt, P. Briozzo, E. Caminade, N. Joly, C. Madzak, C. Mougin, Biochemistry 41 (2002) 7325;
(d) K. Piontek, M. Antorini, T. Choinowski, J. Biol. Chem. 277 (2002) 37663;
(e) S.A. Roberts, A. Weichsel, G. Grass, K. Thakali, J.T. Hazzard, G. Tollin, C. Rensing, W.R. Montfort, Proc. Natl. Acad. Sci. U.S.A. 99 (2002) 2766;
(f) F.J. Enguita, L.O. Martins, A.O. Henriques, M.A. Carrondo, J. Biol. Chem. 278 (2003) 19416.

[40] (a) L.-E. Andréasson, R. Brändén, B.G. Malmström, T. Vänngård, FEBS Lett. 61 (1976) 115;
(b) L.-E. Andréasson, R. Brändén, B. Reinhammar, Biochim. Biophys. Acta 438 (1976) 370.

[41] (a) R. Aasa, R. Brändén, J. Deinum, B.G. Malmström, B. Reinhammar, T. Vänngård, FEBS Lett. 61 (1976) 115;
(b) R. Aasa, R. Brändén, J. Deinum, B.G. Malmström, B. Reinhammar, T. Vänngård, Biochem. Biophys. Res. Commun. 70 (1976) 1204.

[42] V.S. Langford, B.E. Williamson, J. Phys. Chem. A 101 (1997) 3119.

[43] B.D. Liboiron, J. Yoon, R. Sarangi, B. Hedman, K.O. Hodgson, E.I. Solomon, in preparation.

[44] E.I. Solomon, M.A. Hanson, in: E.I. Solomon, A.B.P. Lever (Eds.), Inorganic Electronic Structure and Spectroscopy, John Wiley & Sons, New York, 1999, p. 1.

[45] E.I. Solomon, E.G. Pavel, K.E. Loeb, C. Campochiaro, Coord. Chem. Rev. 144 (1995) 369.

[46] (a) P.J. Stephens, J. Chem. Phys. 52 (1970) 3489;
(b) G.A. Osborne, P.J. Stephens, J. Chem. Phys. 56 (1972) 609.

[47] (a) P.J. Stephens, Annu. Rev. Phys. Chem. 25 (1974) 201;
(b) S.B. Piepho, P.N. Schatz, Group Theory in Spectroscopy with Applications to Magnetic Circular Dichroism, John Wiley & Sons, New York, 1983.
[48] F. Neese, E.I. Solomon, Inorg. Chem. 38 (1999) 1847.
[49] B.S. Gerstman, A.S. Brill, J. Chem. Phys. 82 (1985) 1212.
[50] A.A. Gewirth, E.I. Solomon, J. Am. Chem. Soc. 110 (1988) 3811.
[51] A.B.P. Lever, Inorganic Electronic Spectroscopy, Elsevier, Amsterdam, 1984, p. 553.
[52] N. Lehnert, R.Y.N. Ho, L. Que Jr., E.I. Solomon, J. Am. Chem. Soc. 123 (2001) 8271.
[53] L. Rulíšek, E.I. Solomon, U. Ryde, Inorg. Chem. 44 (2005) 5612.
[54] (a) R. Brändén, J. Deinum, M. Coleman, FEBS Lett. 89 (1978) 180;
(b) R. Brändén, J. Deinum, FEBS Lett. 73 (1977) 144.